FINAL REPORT

for

OGO-6 GAS-SURFACE ENERGY TRANSFER EXPERIMENT

(8 August 1968 - 31 December 1973)

Contract No. NAS5-11163

Prepared by

D. McKeown, R.S. Dummer, J.M. Bowyer, Jr.,
and W.E. Corbin, Jr.

Faraday Laboratories Inc.
La Jolla, California

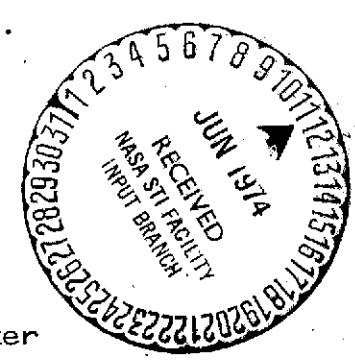

For

Goddard Space Flight Center
Greenbelt, Maryland

FINAL REPORT

for

OGO-6 GAS-SURFACE ENERGY TRANSFER EXPERIMENT

(8 August 1968 - 31 December 1973)

Contract No. NAS5-11163

Prepared by

D. McKeown, R.S. Dummer, J.M. Bowyer, Jr.,
and W.E. Corbin, Jr.

Faraday Laboratories Inc.
La Jolla, California

For

Goddard Space Flight Center
Greenbelt, Maryland

TABLE OF CONTENTS

TABLE OF CONTENTS

LIST OF ILLUSTRATIONS

LIST OF ILLUSTRATIONS

FOREWARD

A gas-surface Energy Transfer Experiment was flown on OGO-6 to measure the kinetic-energy flux of the upper atmosphere relative to the orbiting satellite.[1,2] Energy transfer between 10 microwatts/cm^2 and 0.1 W/cm^2 was measured by short-term frequency changes of temperature-sensitive quartz crystals used in the energy transfer probe.[3] The condition of the surfaces was continuously monitored by a quartz crystal microbalance to determine the effect surface contamination had on energy accommodation.

Results from the experiment provided the first direct measurements of upper atmospheric interactions with surfaces,[4] as well as, new data on surface contamination.[5] Measurements showed that the energy transfer by the upper atmosphere to surfaces could be readily measured below 500 km. The energy flux varied greatly from day to night and with altitude and reached a maximum value of 110 microwatts/cm^2 at the 400 km perigee of OGO-6. Contamination outgassing primarily from the solar panels significantly modified the aluminum surfaces.[6] Theoretical analysis had predicted energy-accommodation coefficients for aluminum of 0.9 but contamination limited this value to 0.2.

The knowledge gained from the experiment has lead to two new instruments for space measurements. One instrument is the Upper Atmospheric Density Gauge.[7] The other instrument is the Thermoelectrically-Cooled Quartz Crystal Microbalance for measuring surface contamination as a function of temperature.[8]

Much of the data obtained from the experiment has been published.[1-7] This Final Report covers analysis not previously reported and new work completed this year. The Report is divided into three parts.

Part 1 is entitled "Gas-Surface Interaction Studies". Results are given on the computer analysis and laboratory tests performed to optimize the operation of the energy transfer probe flown on OGO-6.

Part 2 is entitled "Bombardment of OGO-6 Surfaces by High-Energy Particles". Data are given on the penetration and trapping of protons in surfaces at energies up to an MeV.

Part 3 is a paper entitled "Thermoelectrically-Cooled Quartz Crystal Microbalance" recently presented at the 7th Conference on Space Simulation, Los Angeles, California, November 1973. This new microbalance is to be used to monitor contamination on the Space Shuttle. Its development was partially funded by the NASA Marshall Space Flight Center under Contract NAS8-27879.

PART I

GAS-SURFACE INTERACTION STUDIES

D. McKeown, J.M. Bowyer, Jr. and R.S. Dummer

GAS-SURFACE INTERACTION STUDIES

D. McKeown, J. M. Bowyer, and R. S. Dummer

1.0 INTRODUCTION

When a molecular beam is reflected from a surface, it gives up part of its kinetic energy as a result of the interaction. At energies below a few hundred eV, most of the energy transferred is released as heat since atoms ejected from the surface by the beam will carry little of the energy[1,2] away. In studying molecular beam interactions it is important to know what fraction of the energy is transferred. If the amount of energy transferred can be measured, the accommodation coefficient of the surface can be determined and the nature of the interaction better understood.

The usual way of measuring energy transferred is by attaching a thermocouple to the target. This approach works well at high beam energy but at energies below one keV it does not have the required sensitivity. We have found as a result of working with quartz crystals to measure sputtering[3] that energy transfer can also be detected by a crystal because its oscillating frequency is temperature dependent.[4] By using special cuts of quartz, temperature changes of 10^{-4}°C can be measured.

There are several advantages in using quartz crystals to measure energy transfer. Quartz dissipates heat poorly and a small heat flux will produce a relatively large increase in the temperature of a crystal. Many different materials can be plated or bonded onto quartz. It is a stable substance and can be used in a vacuum at high temperatures. Its frequency-temperature coefficient remains relatively constant down to 0°K. Experiments are performed by placing a crystal in a molecular beam and measuring the energy transferred to it by monitoring changes in its oscillating frequency.[5]

2.0 ENERGY TRANSFER

The rate of change of the crystal temperature due to molecular impacts is:

$$dT/dt = (\alpha E - H)/mc_p \qquad (1)$$

The accommodation coefficient, α, is the fraction of the beam energy transferred to the crystal. The energy, E, carried by the beam, and the heat, H, dissipated by the crystal are in watts. The mass of the crystal is m in g, and c_p is its heat capacity in J/g°C.

A drawing of the crystal is shown in Fig. 1. One side of the crystal is plated with the test material on which energy transfer measurements are to be made. If the plating is a conductor, it can also be used as one of the electrodes needed to drive the crystal in oscillation, otherwise, a conducting electrode must be first plated onto the crystal. The total amount of material that can be plated on a crystal before it significantly damps its oscillation is approximately 10,000 Å for a light material such as aluminum and 1,000 Å for a heavy material such as gold. Nearly the entire surface of the crystal is

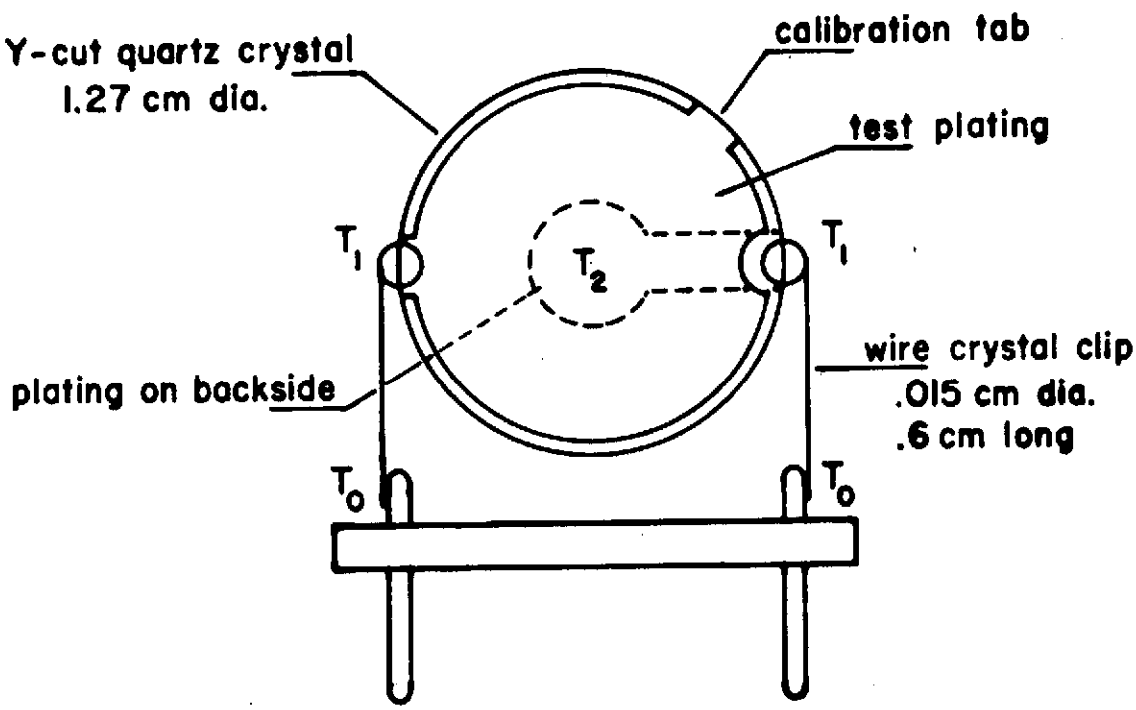

Fig. 1 Quartz crystal temperature sensor

plated to permit measurements with beams having a circular cross section of up to 0.1 cm in diameter.

Another electrode must also be plated on the backside of the crystal, to complete the driving circuit. It has a radius of 2 mm as measured from the center of the crystal so as to keep the plating capacity low and assure a good oscillating amplitude.

The calibration tab is used to drive an electrical current through the plating so that the frequency change of the crystal can be determined when a known amount of power is dissipated at its surface.

$$H = (k_1 a_1/s_1 + k_2 a_2/s_2)(T_2 - T_1) + (k_3 a_3/s_3)(T_1 - T_0) + \sigma(T_2^4 - T_0^4) \quad (2)$$

The heat conductivity of quartz, the plating, and wires holding the crystal are k_1, k_2, and k_3 respectively in J/°C cm sec. The cross sectional area normal to the heat flow is a_1, a_2, and a_3 in cm^2. The conducting path length along the direction of heat flow is s_1, s_2, and s_3 in cm. The temperature at the center of the crystal where the beam impacts is T_2. The temperature at the edge of the crystal is T_1, and T_0 is the ambient temperature. The Stefan-Boltzmann constant is σ.

For short bombardment periods $H \approx 0$, and the energy transferred to the crystal can be found from measuring its temperature change. It was calculated that for a bombardment period $T < 10$ sec, $H < .03\,\alpha E$ and,

$$\alpha E = mc_p\, dT/dt \quad (3)$$

to within 3 percent.

Knowing the energy carried by the molecular beam, the accommodation coefficient can also be found and:

$$\alpha = (mc_p/E)\, dT/dt \quad (4)$$

Experimentally it was shown that the energy dissipated by the crystal over short periods is much less than the energy transferred from the beam for temperachanges of less than one °C. By limiting the input of electrical power to 1 mW/cm^2, the first 10 seconds of data is within a few percent of the calculated linear frequency increase.

3.0 THERMAL ANALYSIS OF THE ENERGY TRANSFER PROBE

A thermal analysis was made on the energy transfer probe to optimize its operation. The probe utilizes an oscillating quartz crystal as the temperature sensor. Fig. 2 shows the probe. Four of these probes were flown on OGO-6. The probe was pointed into the upper atmosphere stream and when the shutter is opened, impacts of molecules transfer energy to the sensor crystal, raise its temperature, and cause its oscillating frequency to change. The change in frequency is proportional to the energy transferred. From the frequency change the accommodation

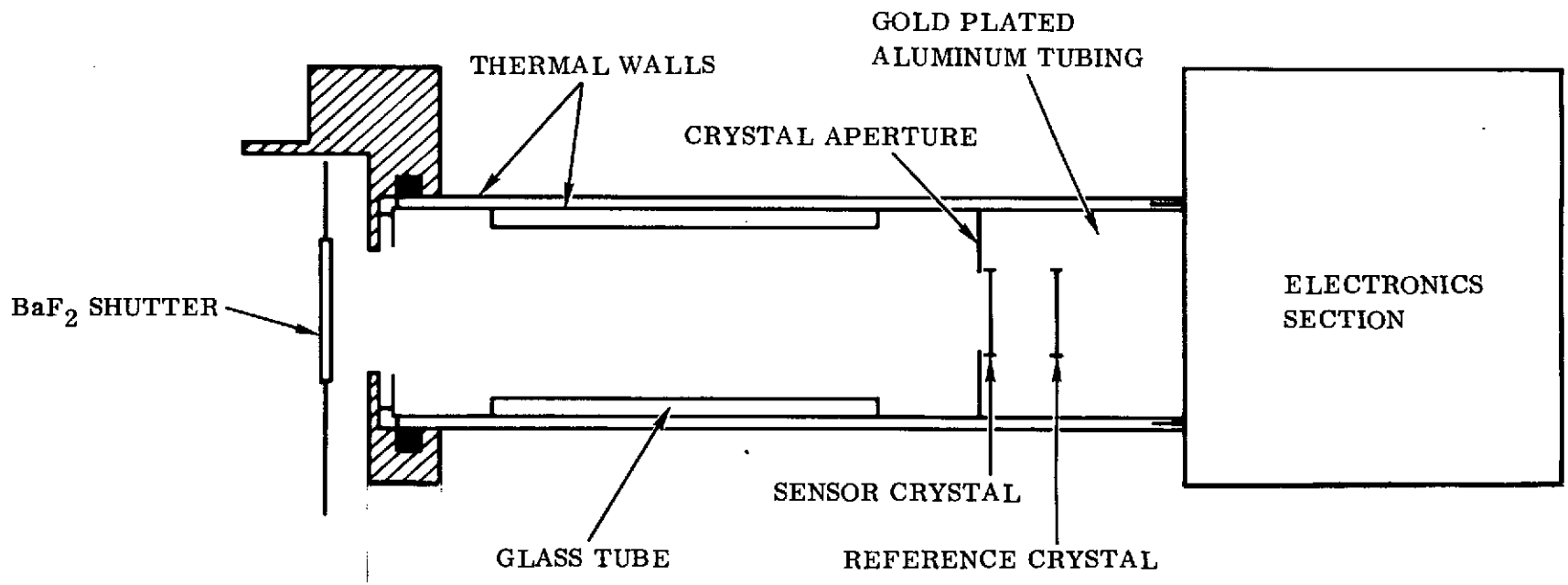

Fig. 2 OGO-6 Energy Transfer Probe

coefficient of the surface plated on the crystal can be determined. The analysis includes the use of a BaF_2 shutter so that the probe can be used in later work now being planned with neutral beams.

Thermal analysis of the probe was accomplished by dividing it into a network of thermal nodes. The nodal network was solved by the solution of a set of linear first order differential equations.

Design goals were:

a. Optimize plating of the crystal sensor to reduce radiation losses.
b. How best to coat instrument walls to reduce space temperature effects on the crystal.
c. Effects of electronics leads on heat conduction.

3.1 THERMAL ANALYSIS COMPUTER PROGRAM

The analysis involved the use of several digital computer programs. The term "thermal model" refers to the basic physical parameters of a system which influence its temperature within a given environment. Some of these parameters are:

a. Mass
b. Specific heat
c. Thermal conductivity
d. Thermal radiative surface properties (reflectance, transmittance)
e. Geometrics shape

The probe was divided into parts called nodes. This is usually done on the basis of isothermality. That is, those parts of the object which are considered by the analyst to have a common temperature, due to high internal conduction paths, are lumped together. The degree of accuracy of the calculation procedures is very dependent on this process. In general, the more nodes considered, the more accurate the results.

Temperature is a measure of the stored energy of an object. The process of computing temperature as a function of time is an energy balance between the folling factors:

a. Heat energy lost or gained by conduction to or from another node
b. Heat energy lost or gained by radiation to or from another node
c. Heat energy gained by radiation from the radiative environment
d. Heat gained through molecular energy accommodation to the surface
e. Heat gained by the dissipation of electrical energy as heat within the node
f. Heat lost by radiation to the environment

When the above factors are summed, they produce a net gain or loss of energy to the node. Energy gained is stored in the mass of the node and results in positive change of temperature. This change of temperature is directly proportional to the product of the mass and specific heat of the node. Energy lost to the node results in a negative change of temperature with the same constant of proportionality.

The integration program is a logical procedure for evaluating the heat energy effect on a multinodal object. It can solve systems involving as many as 200 nodes, considering 25 conduction paths and 25 radiation paths to each node. A maximum number of 400 conductive paths and 100 radiative paths is permitted in all.

The program is written for the greater part in the FORTRAN language, which permits easy interpretation or modification for special uses.

3.2 NUMERICAL INTEGRATION

The general equation for the storage of heat in mass is:

$$Q_t = WC \frac{dT}{d\theta} \tag{5}$$

This first order differential equation is replaced with the difference equation, and with some rearrangement yields:

$$\Delta T = \frac{Q_t \Delta\theta}{WC} \tag{6}$$

The Eulerian technique of numerical integration yields the following equation for the advancement of temperature at node (i) and time (θ):

$$T_{(i)\ \theta + \Delta\theta} = T_{(i)\theta} + \frac{Q_{t\ (i)\ \Delta\theta}^{\ \theta}}{W_{(i)}\ C_{(i)}} \tag{7}$$

Temperature values on the interval θ min to θ max converge to the solution of equation (5) for small enough values of $\Delta\theta$.

This numerical procedure is explicit, and convergence must be insured by check runs at smaller intervals of integration. However, if the results plot as smooth curves (stable solution), the solution obtained is usually convergent.

The procedure of equation (7) is applied at every node based on heat flux conditions prevailing at the beginning of the interval. Temperatures for all the nodes and time are advanced to the end of the interval where heat flux calculation can be made based on the new set of temperatures based on the same recursion formula, equation (7).

3.3 HEAT FLUX CALCULATIONS

The following heats are added algebraically to produce Q_t (total heat) at node (i).

The dissipated heat, Q_{dis} in the program, is an input value for each node considered. For those nodes in which no electrical energy is dissipated, the Q_{dis} column is left blank. The value of Q_{dis} is subject to an off-on switch in the environment table. System duty cycles may be simulated in this manner to turn the entire electrical system on or off at predetermined times. Q_{dis} is entered in watts.

Two physical surface properties of materials are important in computing the heat absorbed from the various energy sources mentioned above. These are the radiant energy absorptivity (α) and the thermal emissivity (ϵ) of the node or its surface coating. The absorptivity measures the fraction

of energy absorbed by the node (i), as compared to that absorbed by a black body where the energy source has the spectrum of the sun. The thermal emissivity measures the fraction of energy emitted at node (i) as compared to that emitted by a black body of the same temperature. Where an energy source is in the same temperature range as node (i), the thermal emissivity (ϵ) also measures the fraction of the source energy absorbed as compared to that which would be absorbed by a black body.

The tabular data is interpolated for the proper compute time by the following linear interpolation formulas:

$$S_{(i)}{}^{\theta} = \frac{\theta - \theta_t}{\Delta\theta_t} \left\{ S_{(i)}{}^{\theta_t + \Delta\theta_t} - S_{(i)}{}^{\theta_t} \right\} \tag{8}$$

$$Al_{(i)}{}^{\theta} = \frac{\theta - \theta_t}{\Delta\theta_t} \left\{ Al_{(i)}{}^{\theta_t + \Delta\theta_t} - Al_{(i)}{}^{\theta_t} \right\} \tag{9}$$

$$Th_{(i)}{}^{\theta} = \frac{\theta - \theta_t}{\Delta\theta_t} \left\{ Th_{(i)}{}^{\theta_t + \Delta\theta_t} - Th_{(i)}{}^{\theta_t} \right\} \tag{10}$$

Total environmental heat at time t is then computed by:

$$Q_{E_{(i)}} = {}_{(i)}[S_{(i)} + Al_{(i)}] + \epsilon_{(i)} Th_{(i)} \tag{11}$$

The heat which is exchanged by conduction is computed using:

$$Q_{c_{(j)}} = \frac{K_{(j)} A_{c_{(j)}}}{L_{(j)}} \left\{ T_{a_{(j)}} - T_{b_{(j)}} \right\} \tag{12}$$

where m values of conductivity (K) conductive path cross section (A_c) path length (l), and the integers (a) and (b) are entered as input by the analyst for conductive paths numbered j = 1 - m. The integers (a) and (b) denote the numbers of nodes (i) linked by the conductive path at (j) Block 2 which is called the "Q Table" lists after the designator QC those conduction paths by number (j) which affect node (i). The "Q Table" is developed by the program from conduction and radiation path input data.

Heat which is exchanged by radiation between nodes is computed using:

$$Q_{r_{(k)}} = \sigma \mathcal{F}_{(k)} A_{c_{(k)}} \left\{ T^4{}_{c_{(k)}} - T^4{}_{d_{(k)}} \right\} \tag{13}$$

where m values of script F ($\mathcal{F}$) and the integers c and d are entered for each radiative pat k = 1 → n in the same manner as for conductive paths. The designator QR proceeds the "Q Table" listing of radiative path numbers (k) for nodes (i). The values of ($\mathcal{F}$) are obtained from the script ($\mathcal{F}$)

program when an internal radiosity network is involved. External radiation to space may be handled by setting:

$$\mathcal{F}_{(i)} = F_{(i)}\,\epsilon_{(i)} \tag{14}$$

where F is the geometric view factor of node (i) for space. Space is entered as a dummy node of T = -460°F.

Qt is computed using:

$$Qt_{(i)} = Q_{dis_{(i)}} + QE_{(i)} + \sum_{k}^{i} Q_r + \sum_{k}^{i} QC \tag{15}$$

That is, Qt is the value of electrical power dissipated at node (i) plus the environmental heat at (i), plus the sum of the radiative heats at (i), plus the sum of the conductive heats at (i).

3.4 QUASI STEADY STATE OPTION

For systems which have large variations in the thermal mass $(W_{(i)}C_{(i)})$ of the various nodes, this option may prove of value. Nodes of extremely small thermal mass tend to respond quickly to their thermal environment. Where these light nodes are mixed with other nodes of greater mass, the integration step size ($\Delta\theta$) for convergence is determined by the lighter nodes. This effect sometimes causes excessively long running time for the computer. To avoid this occurance, the analyst may sometimes wish to indicate some nodes as Quasi Steady State Nodes. The program then treats these nodes as though they had no mass at all so that they respond instantaneously to their environment of the moment at each time step. The mathematical procedure used for accomplishing this effect is called Relaxation. The set of differential equations for the Q.S.S. nodes becomes a set of algebraic equations. The temperatures at each node are adjusted by a procedure called "Regula Falsi" to drive the $Q_{(t)}$ for each Q.S.S. node to zero.

3.5 RADIANT EXCHANGE FACTOR PROGRAM

Radiant losses from the Energy Transfer Probe are a function of the emittance and reflectance of the various surfaces which "see" the crystal (Fig. 3). In order to properly analyze the radiation losses to space, the effects of multiple reflection within the probe chamber must be considered. This analysis was performed using a radiant exchange factor program which is described below.

3.6 DEFINITION OF THE RADIATION FACTOR

Radiant energy exchange between elements of a system of non-black bodies may be computed by the following equation:

$$q_{ij} = \sigma F_{ij}\, F_{eij}\, A_i\, (T_i^4 - T_j^4) \tag{16}$$

where,

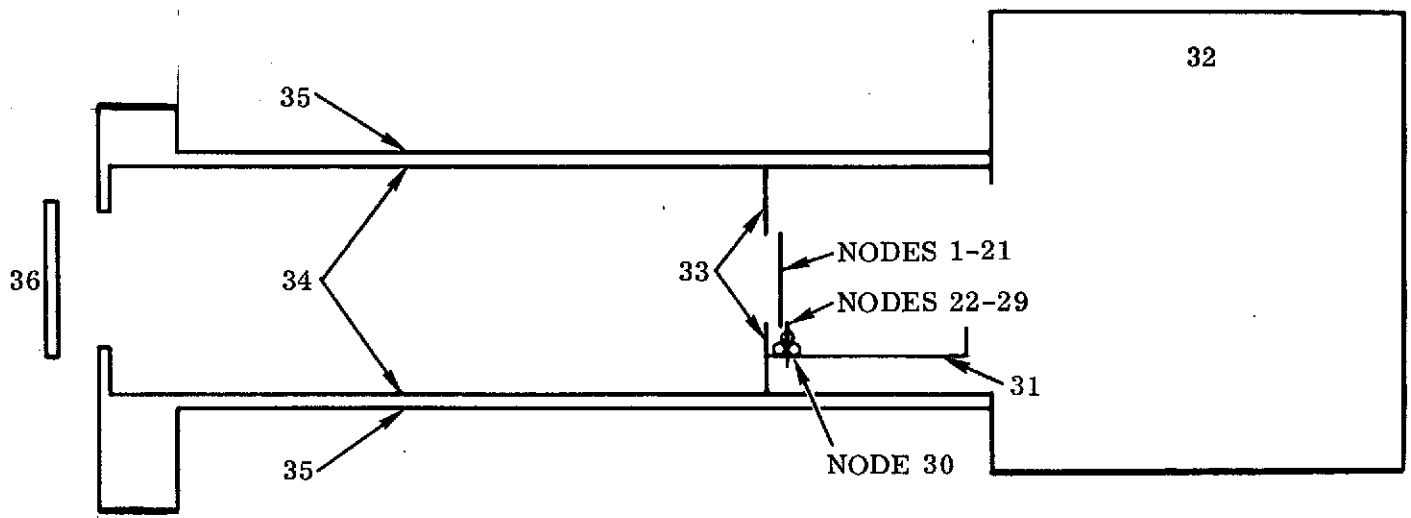

Fig. 3 Thermal nodal diagram of energy transfer probe

σ = the Stefan-Boltzman constant
F_{ij} = the ordinary view factor for black bodies
A_i = the area of the i'th element
T_i = the temperature of the i'th element
T_j = the temperature of the j'th element

F_{eij} is a factor which accounts for the energy transferred between i and j where heat transfer is a function of multiple reflections between i and j themselves and other elements of the system. F_{eij} is a function of both the geometry of the system and the emissivity of the various elements. The product of the geometric view factor F_{ij} and F_{eij} is here called $\mathcal{F}_{ij}$ (called script F). Equation (16) becomes

$$q_{ij} = \sigma \mathcal{F}_{ij} A_i (T_1^4 - T_j^4) \tag{17}$$

3.7 ASSUMPTIONS AND EQUATIONS

The following procedure is adapted, with slight modification, from Gebhardt[6].

The total emission from a non-black surface may be represented by:

$$q_i = \epsilon_i \sigma T_i^4 A_i \tag{18}$$

where ϵ_i = the total hemispherical emissivity of object i.

If B_{ij} is then defined as the fraction of this total energy emitted by element i which is eventually absorbed by j, then the net interchange between i and j can be expressed as:

$$q_{ij} = B_i \epsilon_{ji} \sigma A_i T_i^4 - \epsilon_j \sigma A_j T_j^4 B_{ji} \tag{19}$$

Since, for any geometric system, the following reciprocity relation must hold.

$$B_{ij} \epsilon_i A_i = B_{ji} \epsilon_j A_j \tag{20}$$

By substitution of Equation (20) in (19), Equation (19) becomes:

$$q_{ij} = B_{ij} \epsilon_i A_i \sigma (T_i^4 - T_j^4) \tag{21}$$

By comparison with Equation (17), it is apparent that:

$$\mathcal{F}_{ij} = B_{ij} \epsilon_i \tag{21a}$$

B_{ij} may be determined in the following way. Consider B_{ij}. The total fraction of energy leaving 1 and absorbed by j will be:

$$B_{1j} = F_{1j}\,\epsilon_j + F_{11}\,\rho_1\,B_{1j} + F_{12}\,\rho_2 B_{2j} + \ldots\ F_{1n}\,\rho_n\,B_{nj} \qquad (22)$$

The first term on the right side of Equation (22) represents energy transferred directly, where F_{1j} is the view factor of 1 for j and the total absorptivity of j equals the total emissivity of j.

$$\epsilon_j = \alpha_j \text{ by Kirchoff's law}$$

Here all surfaces are considered "grey bodies" which have the same value of spectral absorptivity at all wavelengths and which also are isotropic emitters.

The third term on the right hand side of Equation (22) is typical of all other terms where F_{12} is the view factor of 1 for 2, ρ_2 is the reflectivity of 2, and B_{2j} is as previously defined. Note that the assumption is made that element 2 reflects energy in the same manner as it emits energy (isotropic emission). That is, that there is no preferential direction for reflection (diffuse reflection). Since an equation similar to (22) may be written for each element of the system, a linear system of equation is defined with some rearrangement of equation (22).

$$\begin{aligned}
(F_{11}\,\rho_1 - 1)B_{ij} + F_{12}\,\rho_2\,B_{2j} + \ldots + F_{1n}\,\rho_n\,B_{nj} &= -\,F_{1j}\,\epsilon_j \\
F_{21}\,\rho_1 B_{1j} + (F_{22}\,\rho_2 - 1)B_{2j} + \ldots + F_{2n}\,\rho_n\,B_{nj} &= -\,F_{2j}\,\epsilon_j \qquad (22a) \\
&\ \ \vdots \\
F_{n1}\,\rho_n\,B_{ij} + \ldots\ldots\ldots\ldots + (F_{nn}\rho_n - 1)B_{nj} &= -\,F_{nj}\,\epsilon_j
\end{aligned}$$

The coefficients of the unknowns may be expressed in matrix fashion by:

$$M_{ij} = F_{ij}\,\rho_j - \delta \qquad (23)$$

where δ is the Kronecker delta.

The n values of B_{ij} for each j are a function of the right hand side column vector $a_{ij} = -\,F_{ij}\,\epsilon_j$. Since, however, n^2 values of B are required for each $j = 1 \rightarrow n$ for which the M matrix does not change, then in

matrix form.

$$B = M^{-1}a \tag{24}$$

where B and a are square matrices of order n.

$$\rho_1 = 1 - \epsilon_1 \tag{25}$$

for opaque grey surfaces.

In order to obtain a square array of $\mathcal{F}$ values for use in Equation (17), each row of the B matrix may be multiplied by the emissivity ϵ_i corresponding to the elements $i = 1 \rightarrow n$.

3.8 . DETAILED THERMAL MODEL

Thermal models were created for both 10 MHz and 15 MHz crystals. A general schematic of the nodal system for the crystal is given in Fig. 4. This schematic applies to the test instrument using 15 MHz crystals. The model using 10 MHz crystals differs somewhat from this. The length of the steel crystal supports were longer for the 10 MHz crystal. The third lead was not well defined for the 10 MHz crystal. The surfaces of the crystals were divided into 21 nodes, conductive paths from the crystal edges to the mounting were divided as shown.

Fig. 5 is a plot of the comparison between laboratory tests on the 10 MHz crystal and a computer simulation made of the same situation. Power dissipation was 760 μ watts. The center curve of this figure shows the laboratory measurements of frequency response when electrical energy was dissipated in the gold plating on the crystal face. A third lead was used to conduct power to the crystal. Unfortunately the heat leak along this wire is not well defined since an alligator clip connector was used. For this reason the model was run assuming

a. no heat leak along the third lead (top curve), and
b. assuming a leak to match that of the support leads.

From this figure it can be seen that the initial slopes of all three curves are well matched. The slight delay in the laboratory curve is due to a slow collection rate for the data acquisition system. It is readily apparent that adjustment of the third lead leak can be used to align the curves almost perfectly.

Fig. 6 compares time temperature response curves for both the 37 node model and the simplified 12 node model of the same device.

Fig. 7 shows the third cycle of computer predicted instrument response to a chopped molecular beam, where 300 $\mu W/cm^2$ are absorbed by the crystal surface. In simulation the instrument was run to steady state with the window open. Then the beam was imposed and the chopper window was allowed to follow its normal cycle. It can be seen that in three cycles the instrument approaches a cyclic equilibrium. Computer runs used during the

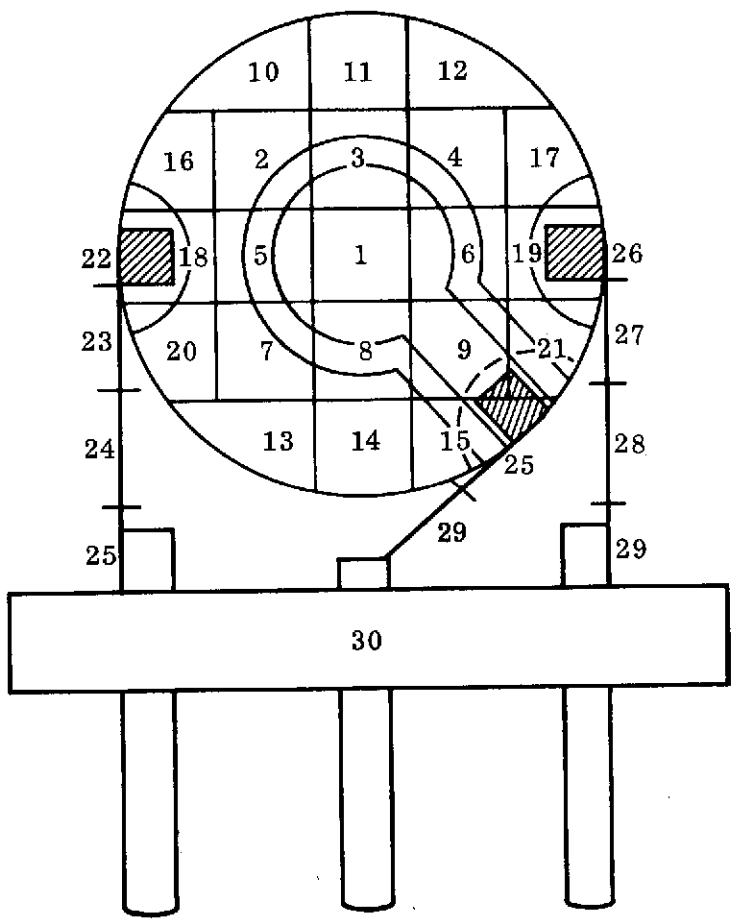

Fig. 4 Thermal nodal diagram of sensor crystal

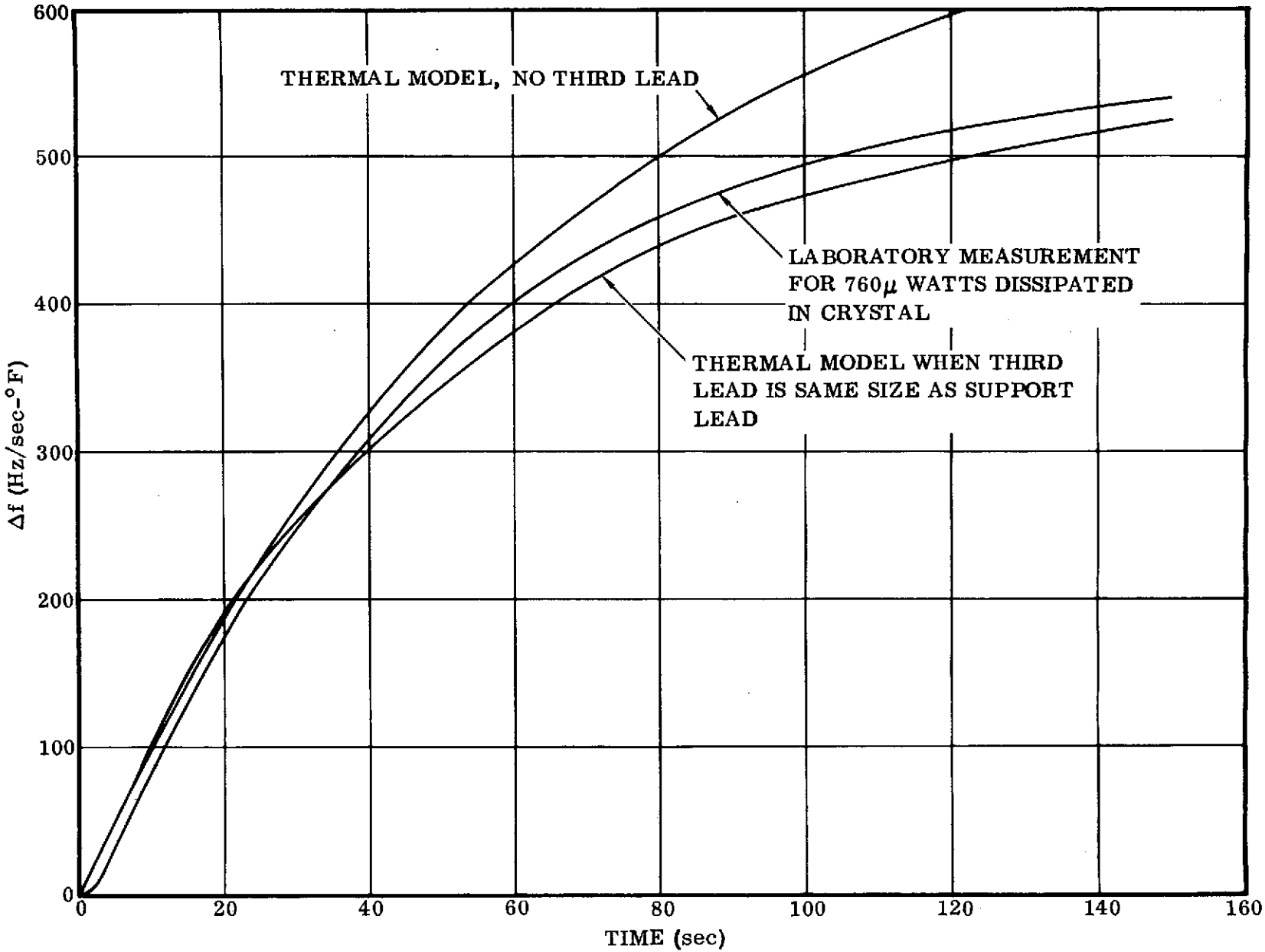

Fig. 5 Frequency response of sensor crystal comparing laboratory measurements with thermal model

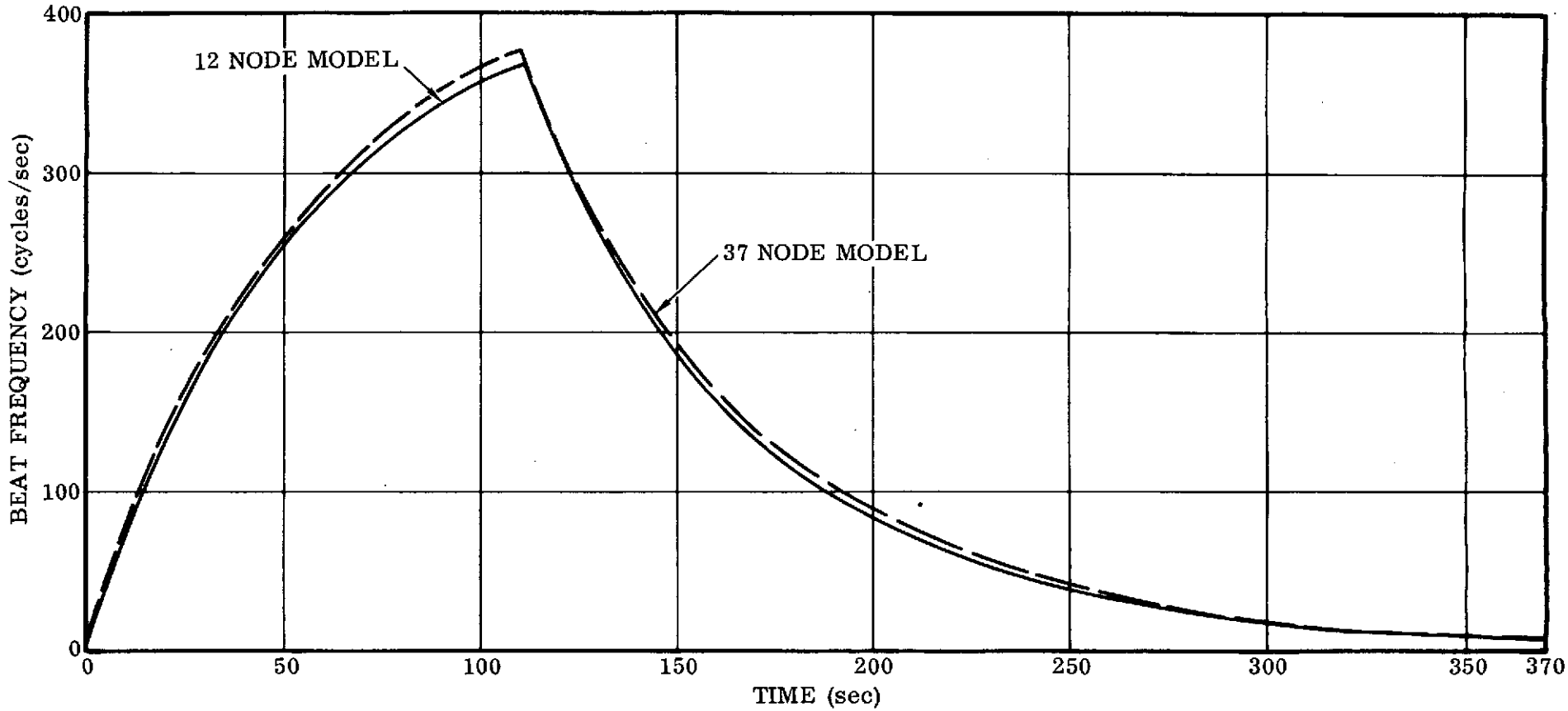

Fig. 6 Thermal model of 15 MHz probe for 300 $\mu W/cm^2$ input

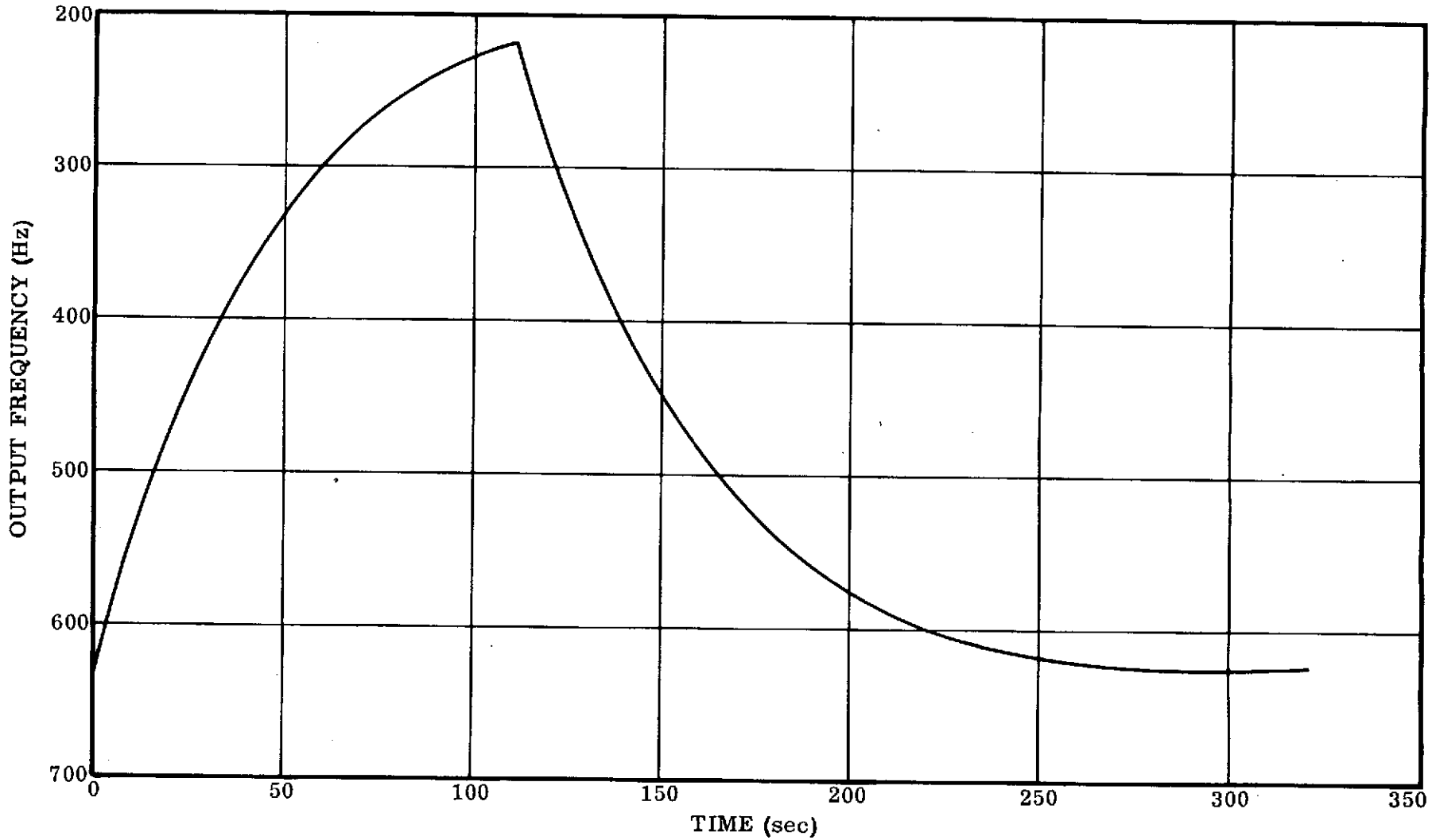

Fig. 7 Probe output for 300 $\mu W/cm^2$ after three cycles of thermal model

study were

a. Run to shutter open equilibrium, no beam
b. First cycle, shutter open, beam on
c. First cycle, shutter closed
d. Second cycle, shutter open
e. Second cycle, shutter closed
f. Third cycle, shutter open
g. Third cycle, shutter closed

4.0 EXPERIMENTAL MEASUREMENTS

With the thermal analysis of the probe completed, experiments were begun on the bombardment of metals in beams of noble gases. Simultaneously, measurements of sputtering yields and kinetic energy transfer rates were made at energies between 50 eV and 600 eV. This energy range is essentially unexplored because most measurements are being done below 10 eV for application to hypersonic flow problems.

Impacts studies between 50 eV and 600 eV are important because this is a transition region where sputtering yields and energy transfer rates increase rapidly with the particle impact energy. This follows because at the low end of the range interactions take place with the first monolayer of target atoms and bombarding particles tend to be reflected with little energy transfer. At the high end of the range, the bombarding particles penetrated a few monolayers into the target and become momentarily trapped and energy transfer is nearly complete.

Measurements were made at normal incidence on polycrystalline Al and Au in Ne^+, and Ar^+ beams. The surfaces were plated on a 1/2 inch diameter mass and temperature sensitive optically-polished quartz crystals. Mass changes of 5×10^{-10} g/cm^2 and temperature changes of 6×10^{-4}° C were detected.

The results for Al in Ne^+ and Ar^+ are shown in Figs. 8 and 9. During the bombardment period of 200 seconds, target temperatures increased by as much as 0.7 °C above the ambient.

Results for the bombardment of Au in Ne^+ and Ar^+ are shown in Figs. 10 and 11.

Data from Figs. 8-11 were used to obtain the energy accommodation and sputtering yields for the ion-target combinations and are shown in Figs. 12 and 13.

4.1 ENERGY ACCOMMODATION

For energies below 600 eV, a classical approach to the computation of the accommodation coefficient to predict experimental results can be used because the de Brolie wavelength is much smaller than the lattice spacing. For the data given here, a Bohr[7] potential with hard-core approximation can be used to describe the collision that occurs between the impacting particle

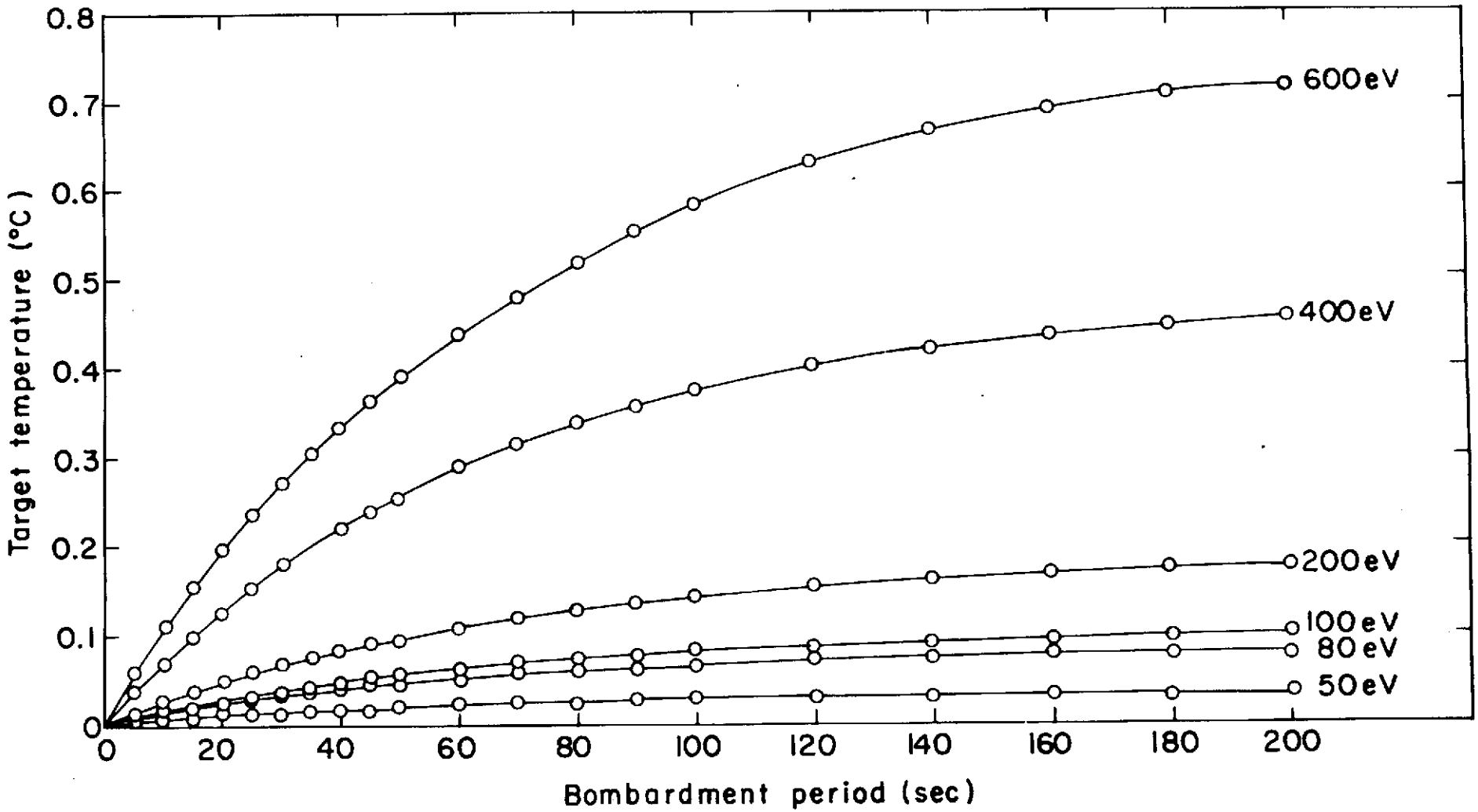

Fig. 8 Temperature rise of Al in a 10 $\mu A/cm^2$ Ne^+ beam at different bombardment energies

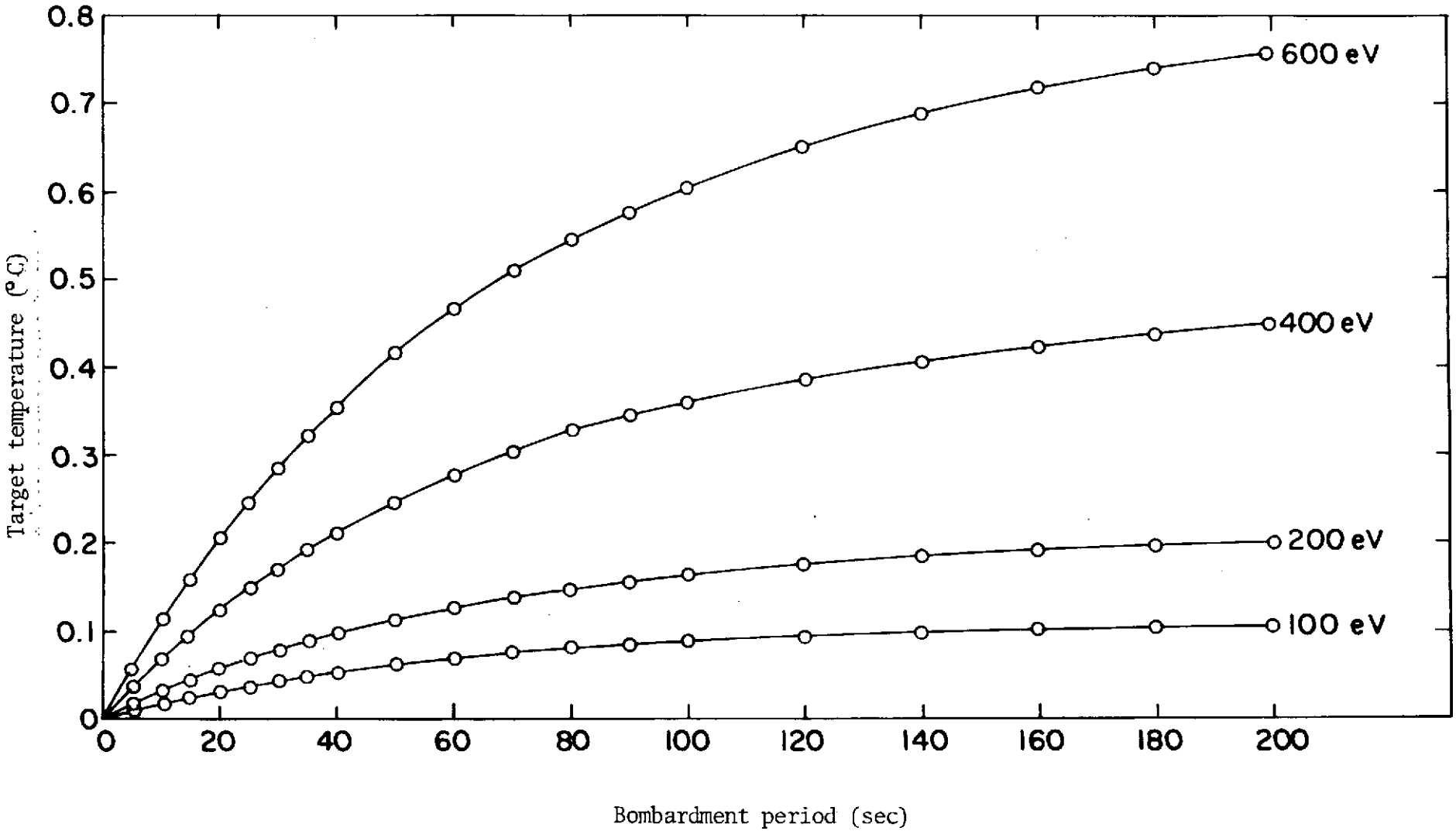

Fig. 9 Temperature rise of Al in a 10 $\mu A/cm^2$ Ar^+ beam at different bombardment energies

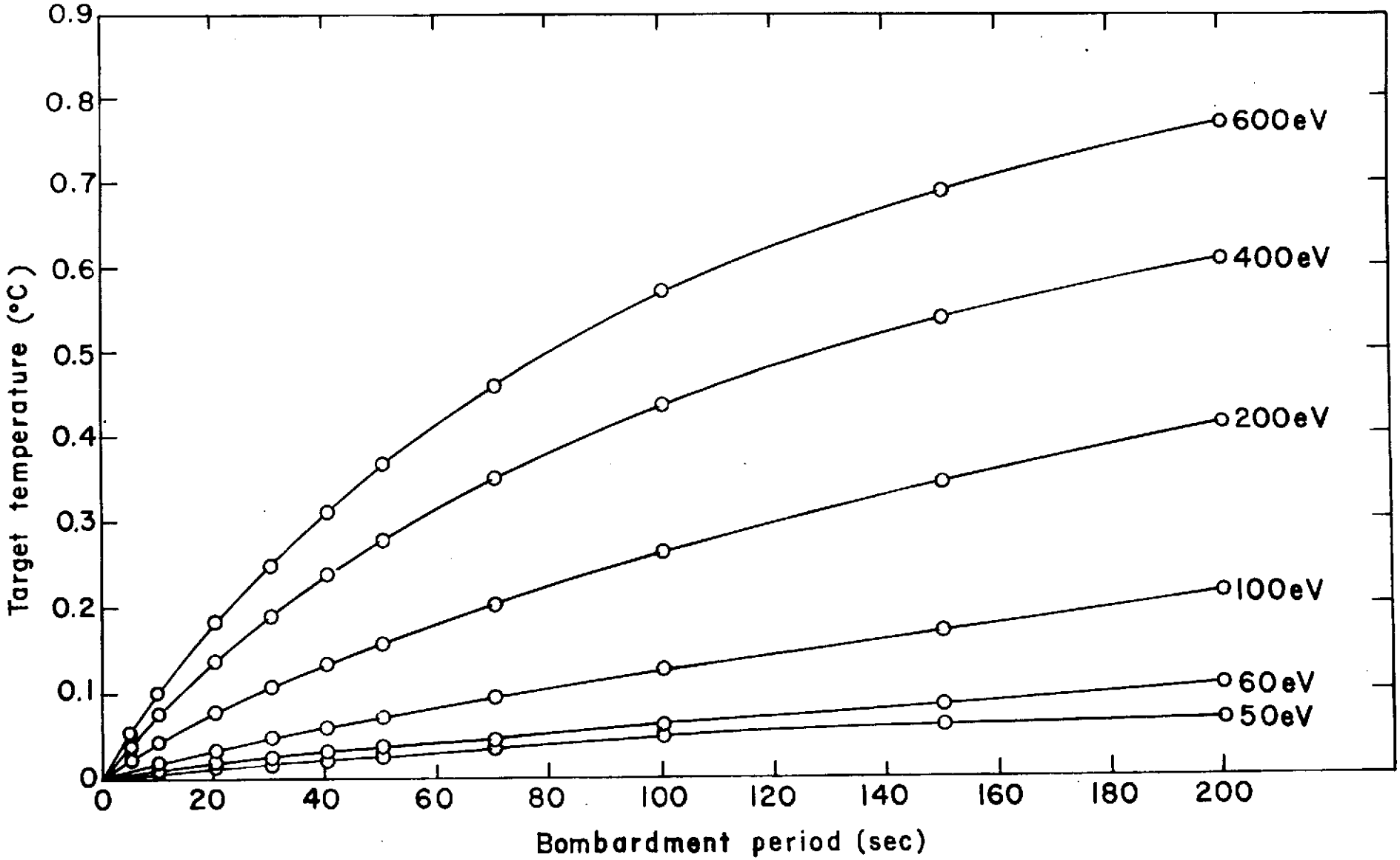

Fig. 10 Temperature rise of Au in a 10 $\mu A/cm^2$ Ne^+ beam at different bombardment energies

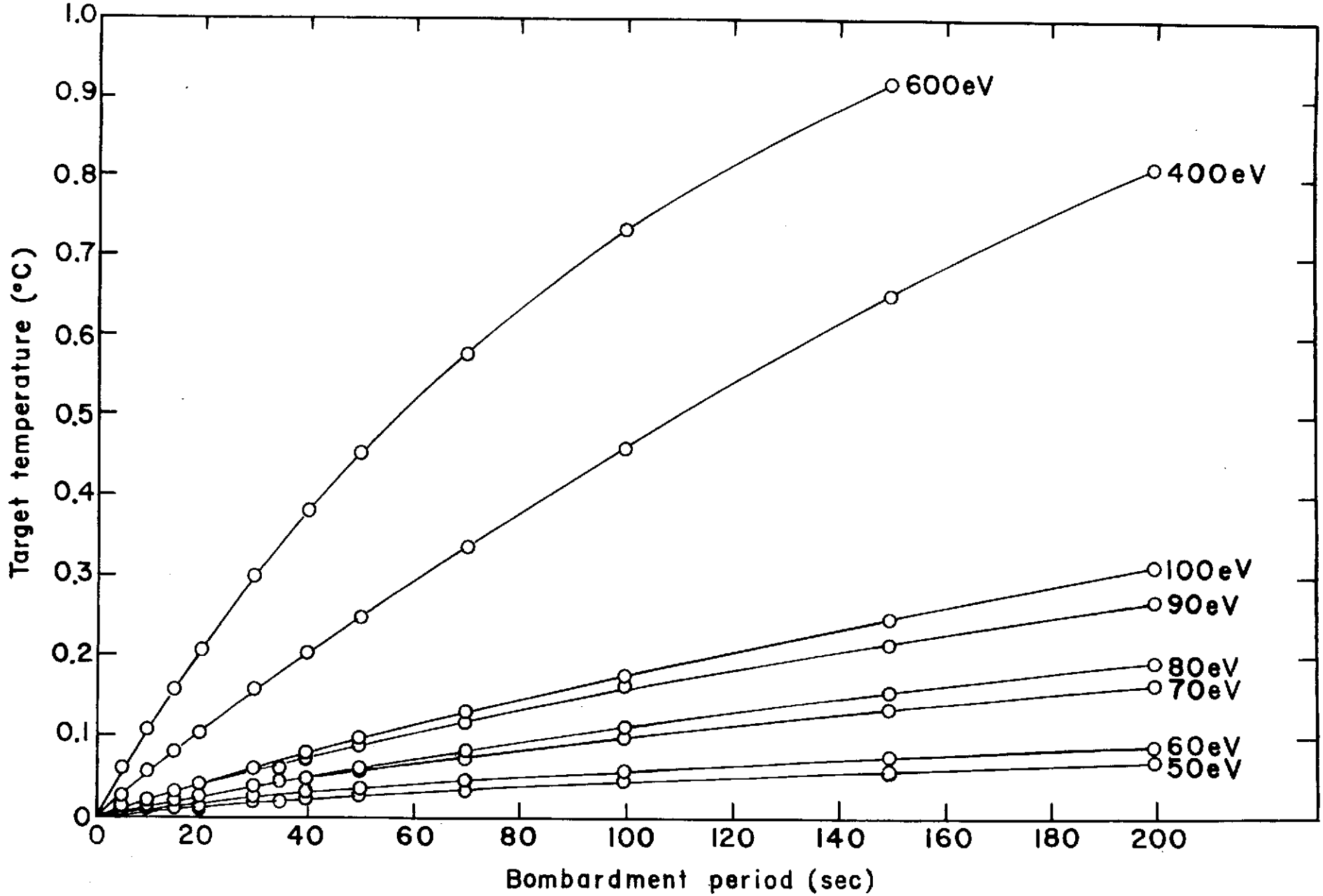

Fig. 11 Temperature rise of Au in a 10 $\mu A/cm^2$ Ar^+ beam at different bombardment energies

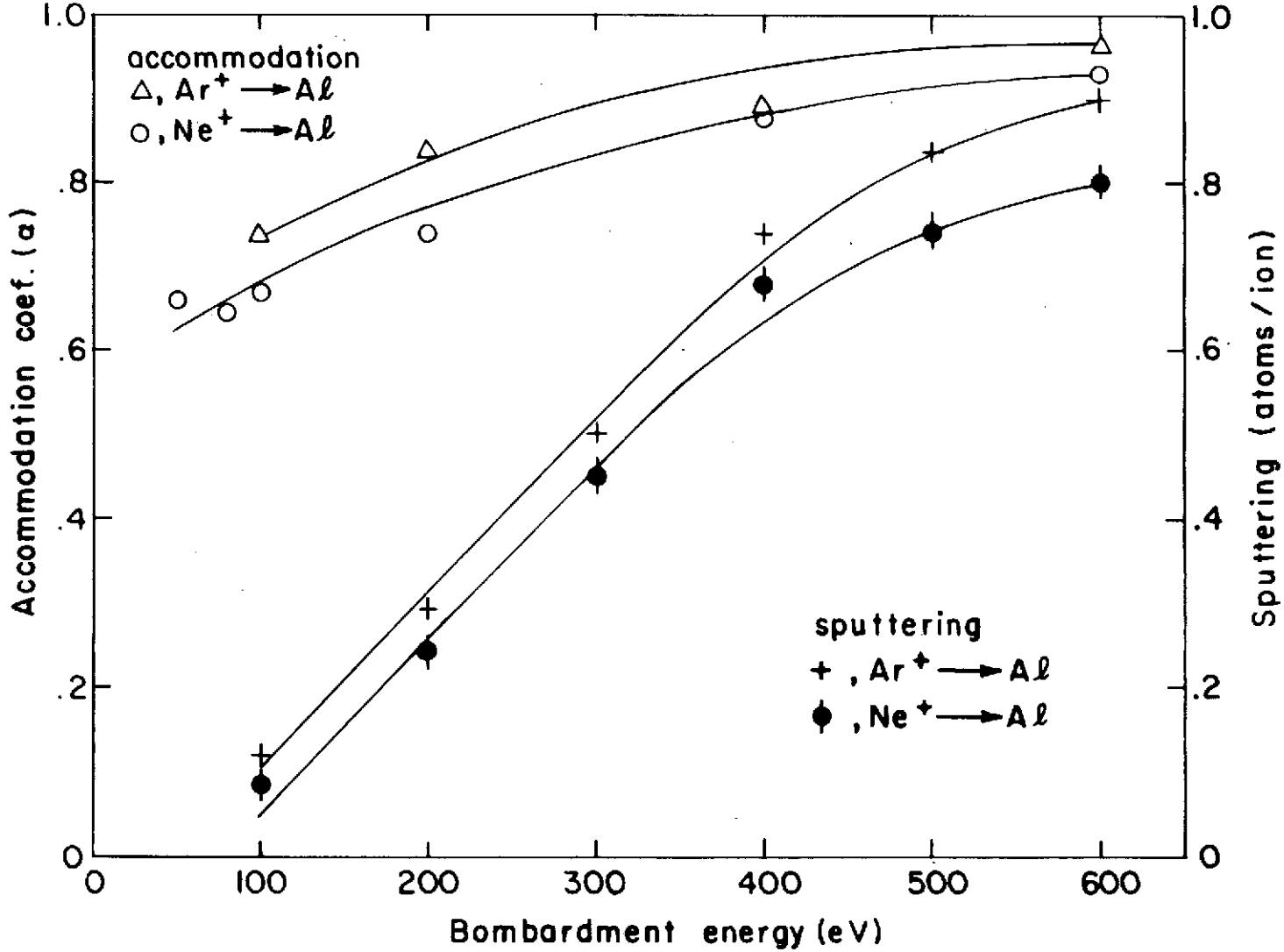

Fig. 12 Sputtering yields and energy accommodation coefficients of Al in Ne^+ and Ar^+ beams

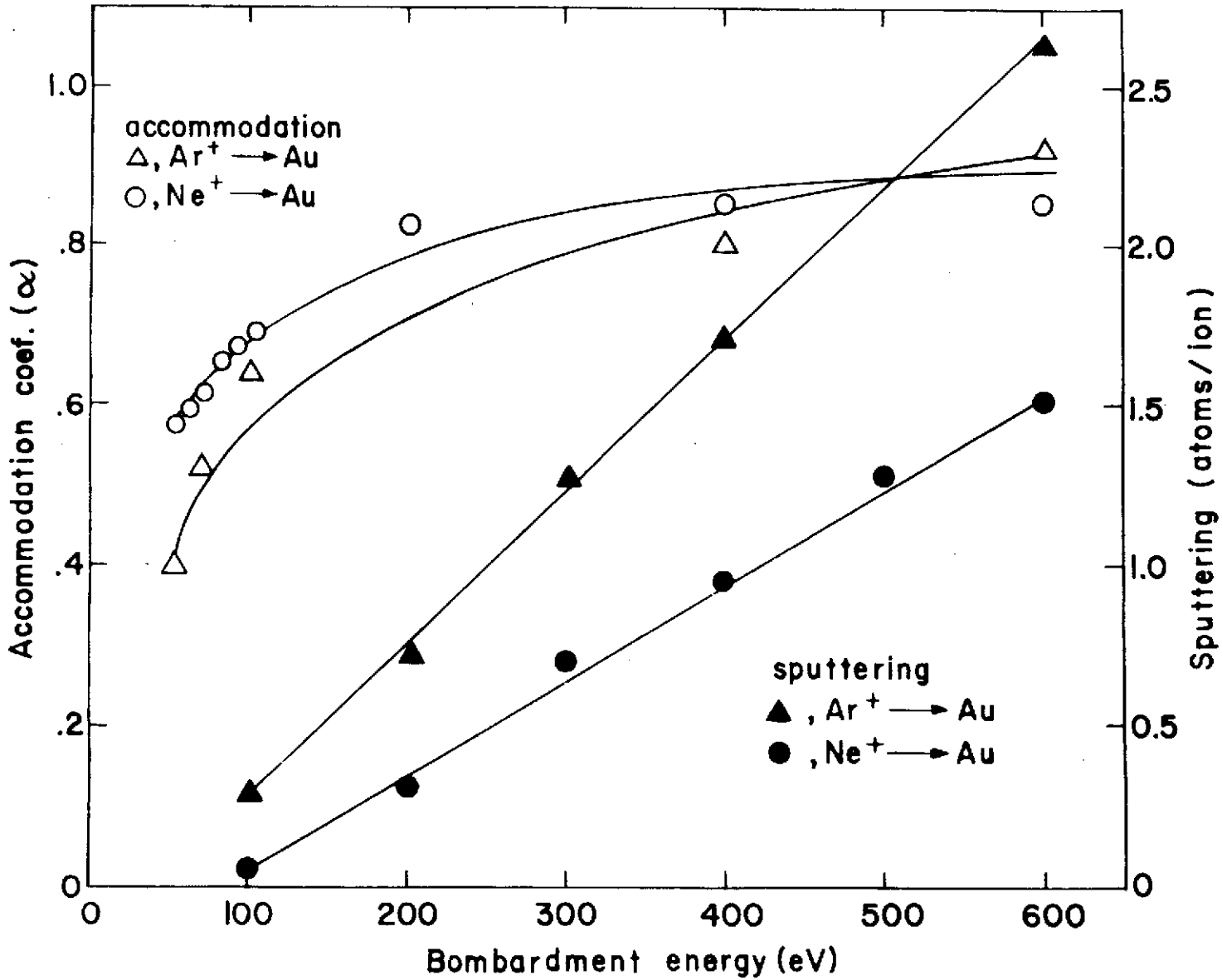

Fig. 13 Sputtering yields and energy accommodation coefficients of Au in Ne^+ and Ar^+

and the target atom.

The transfer of energy is bounded within limits of from zero to $4\,Em_1m_2/(m_1 + m_2)^2$ where the impact energy is E, the incident particle mass is m_1 and the target atom mass is m_2. Taking zero as the lower limit, the resulting average energy transfer is $2\,m_1m_2E/(m_1 + m_2)^2$. By dividing the expression by E, the accommodation coefficient, α, for the surface is obtained. Such an analysis assumes only one collision with the target solid and subsequent return of the incident particle to the gas. Although nearly all of the work reported in the literature has been at energies below 10 eV, a short discussion of this work is valuable here to see how accommodation measurements at low energies compare with our initial results at higher energies.

The simplest theory of how particles transfer energy to a surface was published by Baule[8] in 1914. He applied classical theory and assumed a gas model with a Maxwellian distribution each of which make a single collision with the target solid before returning to the gas, and determined the energy accommodation coefficient, α, to be:

$$\alpha = \frac{2\,m_1m_2}{(m_1 + m_2)^2} \tag{24}$$

Experimental work with low temperature gases has shown marked disagreement with Baule's approximations. Consequently, workers in the field have since become highly sophisticated to bring experiment and theory into closer agreement by considering crystal responses to atomic impact and the attractive and repulsive portions of scattering potentials in addition to the simple hard sphere repulsion.

Theoretical work done by Goodman[9] on the response of a three-dimensional crystal to a normally incident atom fits our experimental work to some degree. He finds the high energy limit for the accommodation coefficient as $4\,m_1m_2/(m_1 + m_2)^2$. This result is not too surprising because only head-on collisions were considered with the collision time much less than the natural period of the crystal lattice. The last condition is tantamount to neglecting the lattice coupling insofar as energy transfer during collision is concerned.

Trilling[10] also considered collisions along the line of centers but allowed all angles of incidence. He computed the accommodation coefficient at high energies $\alpha \approx 1.78\,m_1/m_2$ provided $m_1/m_2 \gg 1$. This result can be understood qualitatively from Goodman's result by averaging over the solid angles of incident direction.

Values in Figs. 12 and 13 reach the maximum energy accommodation given by Goodman at 600 eV. We believe, though, the large transfer of energy resulted from particle trapping and not from neglecting of lattice coupling. Investigations are now being made on the penetration range of impacting particles as a function of impact energy to determine at what energy the impacting particles are effectively trapped.

5.0 REFERENCES (Cited in Foreward)

1. D. McKeown and R.S. Dummer, "Gas-Surface Energy Transfer Experiment for OGO-F", IEEE, Vol. GE-7, No. 2, April (1969).

2. D. McKeown, J.H. Miller, Jr., and M.G. Fox, "Instrument Report for Design of the Gas-Surface Energy Transfer Experiment for OGO-F", General Dynamics Convair, San Diego, Calif., GDC-DBE69-005, Aug. (1969).

3. D. McKeown and M.G. Fox, "Probe for Measuring Energy Transfer between a Satellite and the Upper Atmosphere", Spacecraft Systems, (XVIth International Astronautical Congress), Polish Scientific Publishers, Warsaw (1966).

4. D. McKeown and W.E. Corbin, Jr., "Initial Results from OGO-6 Gas-Surface Experiment, Faraday Laboratories Inc., La Jolla, Calif., FAR-15-69, Oct. (1969).

5. D. McKeown and W.E. Corbin, Jr., "Space Measurements of the Contamination of Surfaces by OGO-6 Outgassing and Their Cleaning by Sputtering and Desorption", Space Simulation, (5th Space Simulation Conference) NBS Special Publication 336, Oct. (1970).

6. D. McKeown and W.E. Corbin, Jr., "Removal of Surface Contamination by Plasma Sputtering", Proceedings AIAA 7th Thermophysics Conference, Univ. Tenn. Space Institute, Tullahoma, Tenn., April (1971).

7. D. McKeown, "Upper Atmospheric Density Gauge", NASA Goddard Space Flight Center Case No. GSC 11,804-1 May (1973).

8. D. McKeown, W.E. Corbin, Jr., and R.J. Naumann, "Thermoelectrically-Cooled Quartz Crystal Microbalance", Space Simulation, (Proceedings of 7th Space Simulation Conference, Los Angeles, Calif.) NASA SP-336, Nov. (1973).

5.1 REFERENCES (Cited in Part I)

1. R.V. Stuart and G.K. Wehner, Transactions of the 9th National Vacuum Symposium, The MacMillan Co., New York, (1962).

5.1 REFERENCES (continued)

2. M. B. Ben'yaminovick and V. I. Veksler, Soviet Phys. - Tech. Physics 9, 284 (1964).

3. D. McKeown, "New method for measuring sputtering in the region near threshold", Rev. Sci. Instr. 32, 133 (1961).

4. W. G. Cody, Piezoelectricity (McGraw-Hill Book Co. Inc., New York, 1946) pp 444-459.

5. D. McKeown and M. G. Fox, "Method for measuring energy transfer from a molecular beam", Rev. Sci. Instr., 36, 656 (1965).

6. B. Gebhardt, Heat Transfer, McGraw Hill Book Co., New York (1961).

7. N. Bohr, The Penetration of Atomic Particles Through Matter, Kgl, Danske Videnskab Selskab. Biol. Medd. 18, No. 8 (1948).

8. B. Baule, "Theoretische Behandlung der Erscheinungen in Verdunnten Gasen", Annalen der Physik, 44, 145-176 (1914). Note: Also available in translated form as B. Baule, "Theoretical Treatment of Phenomena in Rarefied Gases", Annalen der Physik, 44, 145-176 (1914); Royal Aircraft Establishment Library Translation No. 932.

9. F. O. Goodman, "On the Theory of Accommodation Coefficients - III. Classical Perturbation Theory for the Thermal Accommodation of Light Gases", J. Phys. Chem. Solids, 24, 1451-1466, (1963).

10. L. Trilling, "Theory of Gas-Surface Collisions", 392-421, Fundamentals of Gas-Surface Interactions Edited by H. Saltsburg, J. N. Smith, Jr., and M. Rogers Academic Press (1967).

PART II

BOMBARDMENT OF OGO-6 SURFACES BY HIGH-ENERGY PARTICLES

J.M. Bowyer, Jr. and D. McKeown

BOMBARDMENT OF OGO-6 SURFACES BY HIGH-ENERGY PARTICLES

J.M. Bowyer, Jr. and D. McKeown

1.0 INTRODUCTION

At apogee OGO-6 periodically passed through belts of high-energy particles. The particles are composed mainly of electrons and protons. OGO-6 surfaces will be damaged by these particle impacts that will penetrate the surface and displace atoms leading to the discoloration of optical coatings.

When a surface is bombarded by high-energy particles, it will first show a net mass gain from the trapping of particles and then a net mass loss from erosion as successive layers are sputtered by the high-energy impacts. The mass rate of change of the surface, dM/dt, can be expressed as

$$dM/dt = \alpha m_1 i - \beta(t) m_1 - \mu m_2 i \qquad (1)$$

The absorption coefficient α is the fraction of ions that penetrate and become trapped in the target. The re-emission coefficient $\beta(t)$ is the number of trapped particles re-emitted as succeeding layers of target atoms are sputtered. The flux is in particles/cm^2-sec. The number of surface atoms eroded by particle impact is μ. The mass of the bombarding particle and of a surface atom are, respectively, m_1 and m_2. At $t = 0$, $\beta(t) = 0$, and as t becomes large, $\beta(t) \rightarrow \alpha i$. Once $\beta(t) = \alpha i$ the target will lose mass at a constant rate due to sputtering.

To penetrate beyond the first layer of surface atoms, the inequality

$$\sigma n^{2/3} \leq 1 \qquad (2)$$

will hold, otherwise the particle will probably be reflected. With n the atomic number density of the surface, $n^{2/3}$ represents the area number density seen by the incident particle with a total binary cross section, σ. This inequality is satisfied for protons and alpha particles.

Although the cross sections at these low energies are not known accurately, Bohr[1] has shown a reasonable cross section to be

$$\sigma \approx \frac{2\pi a_o^2 E_R}{2.72} \frac{Z_1 Z_2}{(Z_1^{2/3} + Z_2^{2/3})^{1/2}} \frac{m_1 + m_2}{m_2} \frac{1}{E_1} \qquad (3)$$

which is replaced by

$$\sigma = \pi R^2 \qquad (4)$$

whenever $\sigma >> \pi a_o^2/(Z_1^{2/3} + Z_2^{2/3})$. At the lowest energies the binary collision cross section approaches the gas kinetic value. R is the distance of closest approach obtained as the solution of

$$Rm_2E/(m_1 + m_2) = 2Z_1Z_2E_Ra_o \exp[-R(Z_1^{2/3} + Z_2^{2/3})^{1/2}/a_o] \qquad (5)$$

Subscripts 1 and 2 designate incident and surface particles, respectively, with E the kinetic energy, m the mass, A the atomic number, a_o the Bohr radius and E_R the Rydberg energy.

To obtain the distribution of the penetrating ions it is necessary to consider their motion in the surface. Although the ions are probably neutralized upon entering the surface this is expected to be of no consequency since hard sphere type collisions are assumed to occur. For protons and alpha particles, $m_2/m_1 > 1$, large angle scattering occurs at each collision giving an erratic rectilinear path which resembles a diffusion process. In fact, the slowing down process is treated like that of neutrons where the particle slowing down density for a plane flux, i, is

$$q = \frac{i}{(4\pi R)^{1/2}} e^{\frac{-x^2}{4R}} \qquad (6)$$

where R is the "Fermi age".[2] The density, q, represents the number of particles that slow down past an energy, E, at a given depth, x, in the surface. If $m_2/m_1 > 1$, the angular deflection of the incident particle from its direction of travel is small and the particle straggles about the penetration depth with an approximate Gaussian distribution.

Because the notion of range is complex, it is customary to

define a linear, a vector and a projected range. The linear range is the total rectilinear path traversed by the particle to the point of stopping while the vector range is the vector distance from point of entry into the surface to the end point. Projection of the vector distance along a line normal to the surface gives the projected range. An approximate relation between the average linear range R_L and the average projected range R_p (or mean range) was developed by Linhard and Scharff[3] as

$$R_L \approx R_p \left(1 + \frac{1}{3} \frac{m_2}{m_1}\right) \qquad (7)$$

for an inverse square potential. For $m_2 m_1 \leq 1$, approximating (7) is quite accurate but, for $m_2/m_1 > 1$ the approximation has application to a portion of the low energy region only.[4]

Scattering near the end point of the particle travel is probably a man-body collision problem and not the binary one assumed to obtain the distributions discussed in the previous section. If relation (2) is used as a necessary criterion for halting the motion of the incident particle, the cross section must be approximately the gas kinetic value, $\sigma \approx 5 \times 10^{-16}$ cm^2; cross sections of these magnitudes correspong to energies below 1.0 eV for protons and alpha particles. At these low energies the de Brolie wave length is comparable to the lattice separation indicating that more than one target atom contributes to a collision.

Andersen and Sigmund[5] have presented a model for non-binary scattering which is of importance at much higher energies than indicated by (2). It recognized the fact that, with such small mean free paths, correlations between successive collisions cannot be neglected in the low energy region. The model assumed involves a set of crystal lattice rows which are resolved into stacked symmetric rings of atoms. The incident particle moves along the symmetry axis of these rings with the projectile-ring interaction as the basic event with the ring presenting an effective potential field to the incident atom.

If the incident particle is aligned along the symmetry axis, close collisions become improbable because the field keeps the particle near the symmetry axis to produce channeling. For the interpretation of penetration distributions known in the literature as "supertails" it is important to investigate the low energy collisions to determine the density of vacancies, interstitials and self-interstitials created. From

this, estimates of further projectile penetration by diffusion after the slowing down process can be made. Using a Born-Mayer potential for each lattice atom, a new reflecting (or stopping) energy replaces the one determined through (2) and is found to be[5]

$$R_{refl} \approx p\,Ae^{-L/a} \tag{8}$$

whenever $m_1 >> m_2$. Constants p and L define the number of particles in the ring and radius of the ring element; A and a are the potential parameters. Reflection energies given by (8) are somewhat higher than those found through (2); for alpha particles in heavy materials, typical estimates are 5-10 eV.

2.0 DIFFUSION OF TRAPPED PARTICLES

Although channeling gives a plausible explanation of penetration of about one micron for these low energy particles, the "supertails" observed[6] extend to depths of several microns. A possible explanation to these deep penetrations is the steady state diffusion approach of Sparks.[7] He assumes the diffusion of vacancies and self-interstitials created by the incident particle is unaffected by the relatively small number of implanted ions. With the bombarding particles forming substitutionals through the annihilation of vacancies two general forms of the integral penetration distributions, $n_s(x)$, result which may be expressed as

$$n_s(x) \propto \exp[-k(x-\ell)];\ x > \ell \tag{9}$$

and

$$n_s(x) \propto \frac{d^{2+r}}{(x-\ell+d)^{2+r}};\ x > \ell\,. \tag{10}$$

The constant, d, depends upon the vacancy density interstitial density and the diffusion coefficient, ℓ, is located approximately at the edge of the stopping region. Distribution (10) normally occurs if vacancies

and self-interstitials are created and annihilated in pairs. For distribution (9) to obtain the vacancies, the self-interstitials must be created at different rates which means that most of the interstitials must be of the bombarding particle type.

3.0 BOMBARDMENT OF ALUMINUM

Laboratory measurements were made on the bombardment of aluminum surfaces by protons to determine the saturation concentration of protons in this material commonly used on OGO-6. The function, q, given by (6) was used to calculate the distribution. The distribution is for the case $m_1 > m_2$. It has a maximum near the surface because of large angle scattering that occurs for the case in which the incident particle mass m_1 is less than the target atom mass m_2.[10]

The mean penetration depth R_p of the particles needed to scale the distribution function can be found from the $\rho - \epsilon$ relationship of Lindhard and Scharff,[11] which relates the range-energy of particles in solids:

$$\rho = R_m \frac{A_2}{(1 + 3A_1)} \frac{166}{(Z_1^{2/3} + Z_2^{2/3})} \frac{A_1}{(A_1 + A_2)^2} \qquad (11)$$

$$\epsilon = \frac{33}{Z_1 Z_2 (Z_1^{2/3} + Z_2^{2/3})^{1/2}} \frac{A_2}{A_1 + A_2} E_1 \qquad (12)$$

where the subcripts 1 and 2 refer to the incident ion and the target atom, and E_1 is the energy of impact in keV.

Davie's group has shown that the $\rho - \epsilon$ relationship is accurate to about 20% for $\epsilon > 10$. Values for ρ, knowing ϵ, have been plotted by them for $0 < \epsilon < 10$ and $0 < \rho < 100$.[12]

The absorption coefficient α was found, experimentally, to be about 0.01.

The saturation concentration of trapped hydrogen in aluminum is shown in Fig. 1.

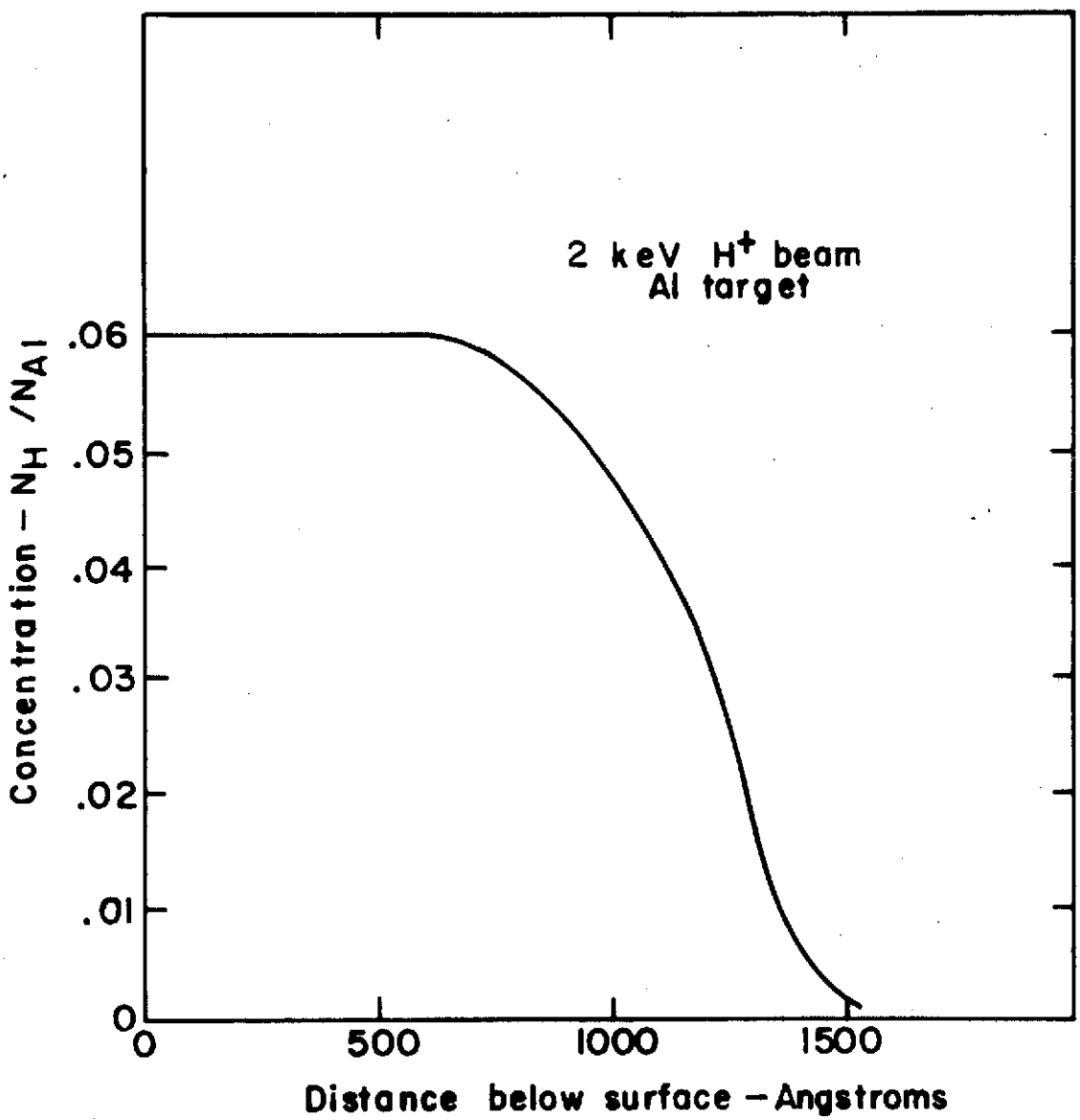

Fig. 1 Saturation concentration of hydrogen

4.0 REFERENCES

1. Bohr, N., "Penetration of Atomic Particles through Matter", Det. Kgl. Dan. Vidensk, Selsk., Mat. - Fys. Medd., Vol. 18, No. 8 (1948).
2. Fermi, E., Nuclear Physics, Chicago, Univ. of Chicago Press, 187 (1956).
3. Linhard, J., and Scharff, M., "Energy Dissipation by Ions in the keV Region," Phys. Rev., Vol. 124, 128 (1961).
4. Linhard, J., Scharff, M., and Schiott, H.E., "Range Concepts and Heavy Ion Ranges," Det. Kgl. Dan. Vidensk. Selsk., Mat. - Fys. Medd., Vol. 33, No. 14 (1963).
5. Andersen, H.H., and Sigmund, P., "Simple Non-Binary Scattering Model Applicable to Atomic Collisions and Crystals at Low Energies," Dt. Kgl. Dan. Vidensk. Selsk., Mat. - Fys. Medd., Vol. 4 (1966).
6. Davies, J.A., and Jespersgard, P., "Penetration of Ions in Solids," Can. J. Phys. Vol. 44, 1631 (1966).
7. Sparks, M., "Theory of Supertails of Ions Bombarded into Crystals," Phys. Rev. Letters, Vol. 17, 1247 (1966).
8. Bergstrom, I., Brown, F., Davies, J.A., Geiger, J.S., Graham, R.L., and Kelly, R., "On the Electromagnetic Separation Method of Preparing Radioactive Sources for Precision β - Spectroscopy," Nucl. Instr. Methods, 21, 249 (1963).
9. Reiffel, L., "Structural Damage and other Effects of the Solar Plasma," ARS J., 30, 258-262 (1960).
10. Nielsen, K.O., "The Ranges of Atomic Particles with Energies about 50 keV," Electromagnetically Enriched Isotopes and Mass Spectrometry, (Academic Press, New York, 1956) pp 68-81.
11. Lindhard, J., and Scharff, M., "Energy Dissipation by Ions in the keV Region," Phys. Rev., 124, 124 (1961).
12. Davies, J.A., McIntyre, J.D., and Sims, G., "The Range of C^{137} Ions of keV Energies in Germanium," Can. Jour. Chem., 40, 1605 (1962).

PART III

THERMOELECTRICALLY-COOLED QUARTZ CRYSTAL MICROBALANCE

D. McKeown, W.E. Corbin, Jr. and R.J. Naumann

THERMOELECTRICALLY-COOLED QUARTZ CRYSTAL MICROBALANCE *

D. McKeown and W.E. Corbin, Jr., Faraday Laboratories Inc., La Jolla, California, and R.J. Naumann, Marshall Space Flight Center, Huntsville, Alabama

ABSTRACT

A quartz crystal microbalance is of limited value in monitoring surface contamination on satellites or in space simulation chambers because it operates several degrees above ambient temperatures. The amount of contamination adsorbed on a surface is highly temperature dependent and the higher temperature of the microbalance will significantly reduce the amount of contamination it adsorbs. Generally, a quartz crystal microbalance will indicate a lower level of contamination than the amount that is actually present. To overcome this problem, a thermoelectrically-cooled quartz crystal microbalance has been developed to monitor surface contamination as a function of temperature.

INTRODUCTION

The use of a quartz crystal microbalance (QCM) is a well established method for weighing thin films of solid materials, down to a fraction of an Angstrom, that are deposited[1] or removed[2] from a surface. Solid films couple strongly into the oscillating QCM and its frequency change is proportional to the mass loading. Direct application of a QCM to monitor a wide range of contamination in space simulation chambers has proven to be a more difficult task because a QCM operates several degrees above ambient temperatures. Gaseous contamination in equilibrium with solid materials in the chamber is not readily adsorbed on a QCM because of its higher temperatures. Contradictory results are often obtained where a passive optical system shows contamination while a QCM operating nearby indicates little is present.

As the study of surface contamination becomes more fundamental in nature, a QCM specifically designed to monitor contamination is

* This work supported under NASA Contracts NAS8-27879 and NAS5-11163. For presentation at the AIAA-NASA/ASTM/IES 7th Space Simulation Conference, November 12-14, 1973, Los Angeles, California

needed. Not only must the heat generated by the QCM be removed, but a convenient method found to automatically control its operating temperature, so that, surface contamination studies can be made over temperature extremes common to spacecraft. To permit in-situ reflectivity measurements, the crystals should be optically polished. With these objectives in mind, a thermoelectrically-cooled quartz crystal microbalance has been developed for monitoring contamination on optical surfaces as a function of temperature.

QCM LIMITATIONS

A QCM is an active quartz crystal oscillator and power dissipation raises its temperature several degrees above the ambient. Because the amount of contamination adsorbed on a surface is highly temperature dependent, a passive surface at ambient temperature will adsorb a number of contamination monolayers until it reaches an equilibrium with sources in the chamber while a QCM will adsorb a smaller number because of the different equilibrium condition. In some cases, a heavily driven QCM will operate about 10°C above ambient. At this elevated temperature no measureable amount of contamination will be observed.

The amount of contamination adsorbed on a surface is dependent on the residence time, τ, of the contamination molecules[3].

$$\tau = \tau_o \exp (\Delta E/RT)$$

where τ_o is the vibrational period of the contamination lattice, ΔE the desorption activation energy, R the gas constant and T the absolute temperature. Griffith[4] has shown that the desorption rate of contamination with desorption activation energies of less than 25,000 cal/g-mol (oils and epoxies) is highly dependent on temperature. A 10°C temperature rise can result in nearly a ten fold increase in the desorption rate. Use of a QCM to monitor contamination will consistently give lower readings than the actual level present because of its higher temperature.

The strong effect of temperature on the adsorption and desorption of contamination is shown in Fig. 1. Here long-term OGO-6 measurements are shown correlating QCM contamination loading to the eclipse period of the satellite. As has been previously reported, the primary source of contamination on the satellite was the solar panels baking out in the sun[5].

OGO-6 was inserted into a polar orbit with its orbit plane normal to the earth-sun line. This orbit was chosen so that the satellite would

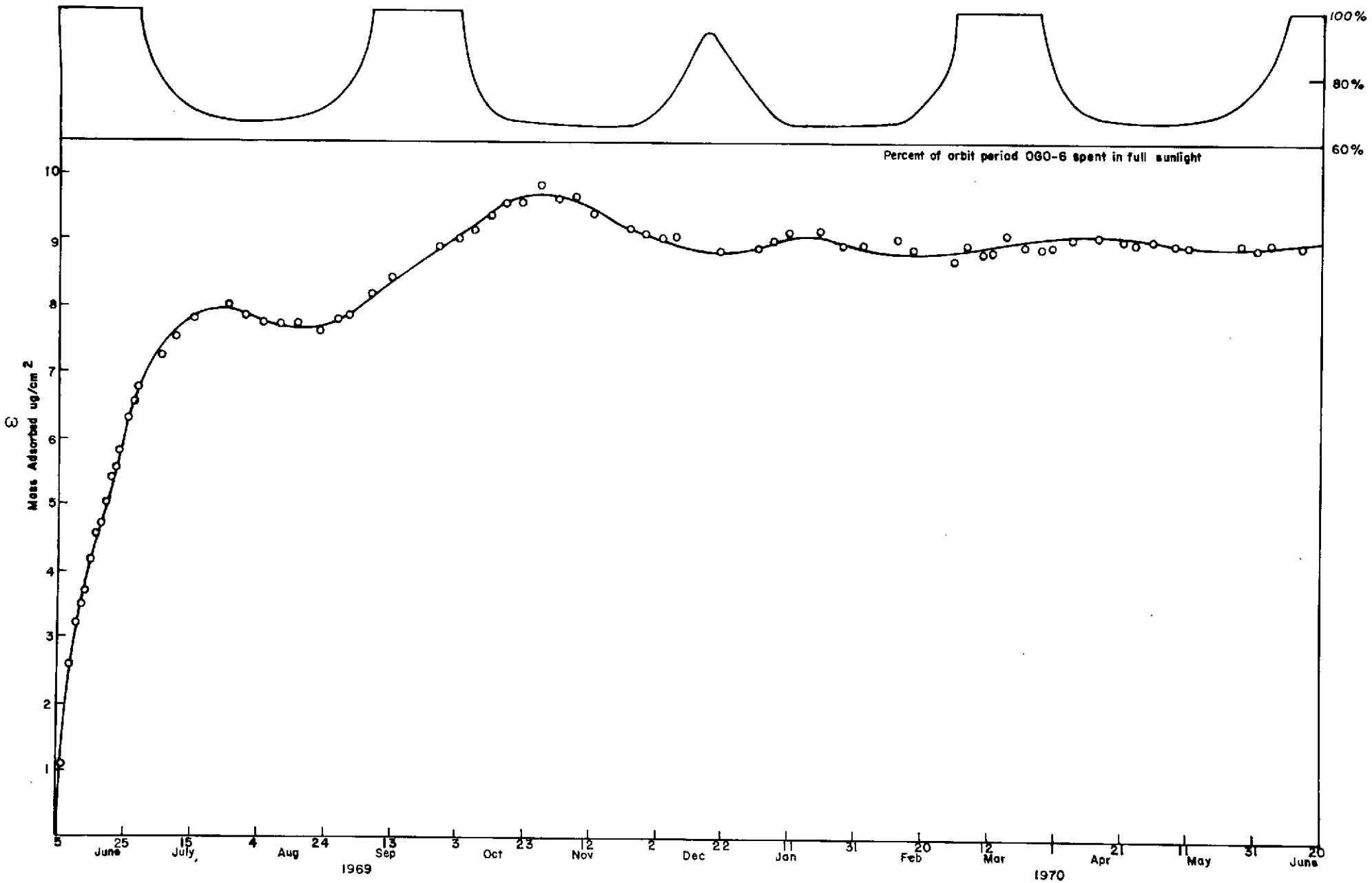

Fig. 1 Long-term OGO-6 surface contamination measurements correlated to the eclipse periods of the satellite

be in full sunlight for the maximum period after launch. During the four week period after launch, the amount of contamination adsorbed onto the QCM steadily increased until the first week in July when it abruptly decreased and finally in August the QCM showed a net loss of contamination and became a contamination source. By correlating the eclipse periods of the satellite to the QCM measurements, the reason for the fluctuation in the contamination adsorption and desorption rates became apparent.

In full sunlight the temperature of the solar panels was 72°C and a wide range of high and low volatile contamination outgassed from the panels onto the QCM. During maximum eclipse, when OGO-6 was in the earth shadow 30% of the time, the average temperature of the solar panels dropped to 60°C and the contamination flux from the panels decreased significantly. The QCM lost contamination during the eclipse period because the lower flux rate from the panels did not balance out contamination desorbing from the QCM. The QCM desorbed contamination into space and onto adjacent surfaces that were at a lower temperature than the QCM.

Although the QCM indicated a loss of contamination during eclipse, contamination was present. Reber's Neutral Mass Spectrometer, located next to the QCM, showed that a strong flux of contamination continued to outgas from the panels.

THERMOELECTRICALLY-COOLED QCM

In order to conduct contamination experiments as a function of temperature, a new instrument called a thermoelectrically-cooled QCM (TQCM) was developed. A thermoelectric device was picked to control temperature because it offers several advantages over other methods. It uses only a series of solid-state bismuth telluride junctions, through which electrical current is passed, to pump heat to or from a load by the Peltier effect. It is small in size and can be remotely operated with a signal pair of electrical leads. It has no moving parts and is highly reliable. There are no requirements for pumping a refrigerant or for supplying a coolant, such as, liquid nitrogen. These features result in greatly reduced operating and maintenance costs in controlling the temperature of a QCM with a thermoelectric device.

The design of the TQCM has been previously reported[6] and only its operation will be described here. The TQCM instrumentation operating under ambient conditions is shown in Fig. 2. The TQCM Controller operates on 115 Vac, 60 Hz at 0.25 A and provides the various voltage outputs to operate the crystal oscillators, temperature bridge,

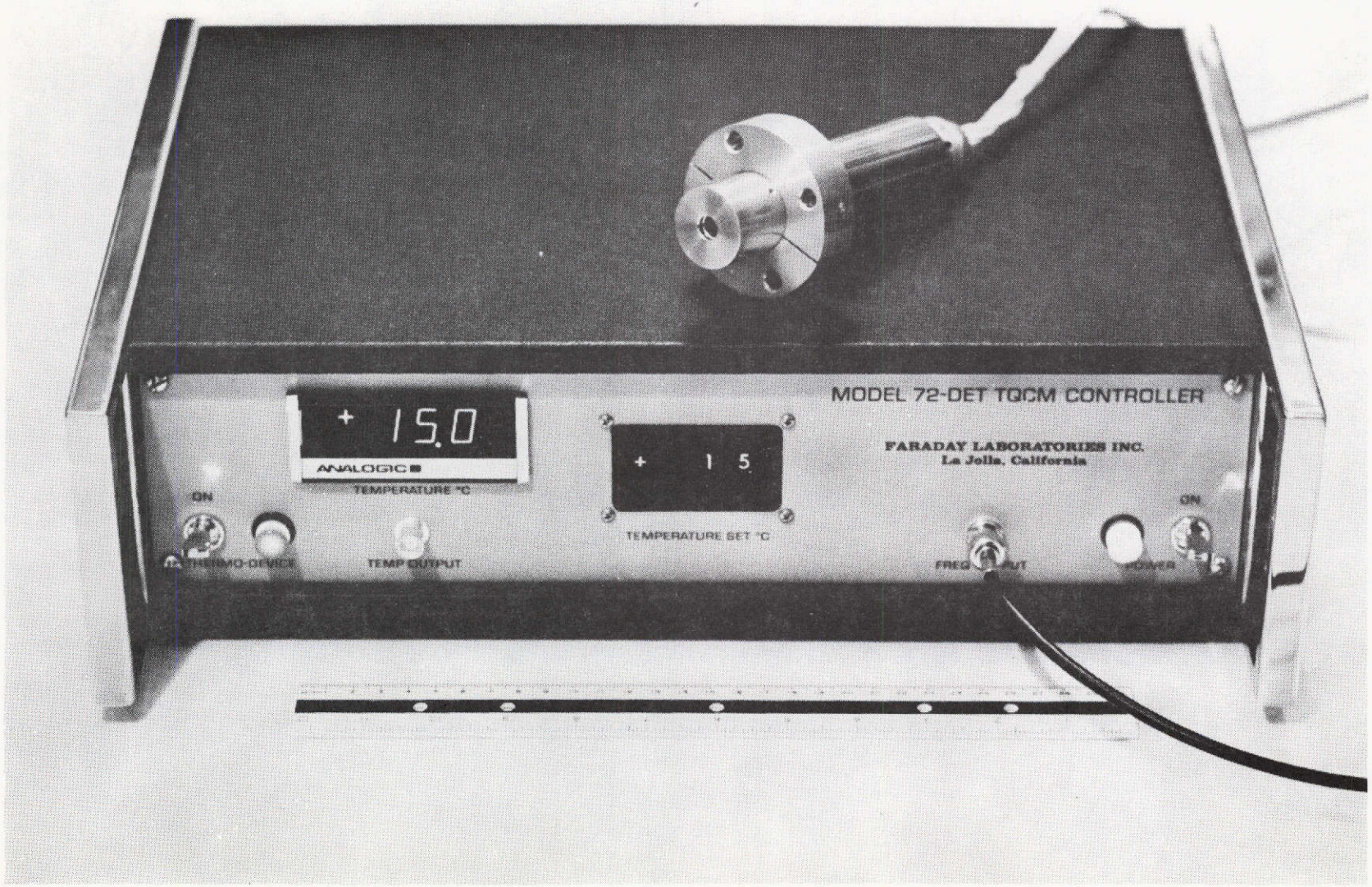

Fig.2 TQCM Operating at +15°C under Ambient Room Conditions

thermoelectric device and readouts of temperature and frequency.

The TQCM Electronics, Heat Sink, and Sensor are shown in Fig. 3. The TQCM uses a two-stage thermoelectric device to automatically control the sensor crystal temperature between -50°C and +100°C to ± 1°C in vacuum. For operation over this range, the heat sink temperature is to be maintained below +40°C. No problem will be encountered in maintaining the heat sink below +40°C by mounting it on a 0.6 cm thick metal bracket. Heat generated by the TQCM is readily dissipated by the bracket at ambient room temperatures.

The TQCM has been designed with an extended temperature bridge circuit and reserve power and will reach a lower temperature limit of -59°C if its heat sink is maintained below +25°C. To maintain a +25°C temperature, the heat sink is to be mounted on a 1.2 cm thick metal bracket capable of removing a maximum 2.8 W when the TQCM is at -59°C. The TQCM cool-down time in vacuum is shown in Fig. 4.

The TQCM operating temperature is set by positioning the thumb wheel switch on the Controller. A 3 1/2 digit panel meter is provided in the Controller for direct readout of temperature.

A temperature output is provided for remote readout or recording. The TQCM temperature sensor is a precision platinum resistance thermometer linear to -.5%. At 100°C the voltage output is 1.00 Vdc. At -59°C the voltage output is - 0.59 Vdc. The TQCM operating temperature in °C equals 100 times the voltage output of the Controller.

A matched pair of precision 10-MHz quartz crystals is used to measure mass loading. The crystals are designated as a sensor and reference crystal. The crystals are optically-polished and plated with Al. The sensor crystal is coated with magnesium fluoride for in-situ reflectivity measurements while contamination is collecting on its surface. The crystals can be changed by unloosening two set screws in the TQCM Sensor.

The output frequency of the TQCM is the beat frequency between the two oscillating crystals. The beat frequency effectively eliminates frequency changes caused by ambient temperature variations. By carefully matching sets of crystals in vacuum, frequency change with temperature of less than ± 50 Hz between -59°C and +100°C is attained. Because only the sensor crystal sees the contamination flux, the TQCM output frequency will increase with mass loading. The crystal sensor is optically polished and full plated on one side. This technique produces a more active crystal whose mass sensitivity is greater by about 20% than semi-polished crystals. The TQCM mass sensitivity, m, is

$$m = 3.5 \times 10^{-9}\ g/cm^2\text{-}Hz$$

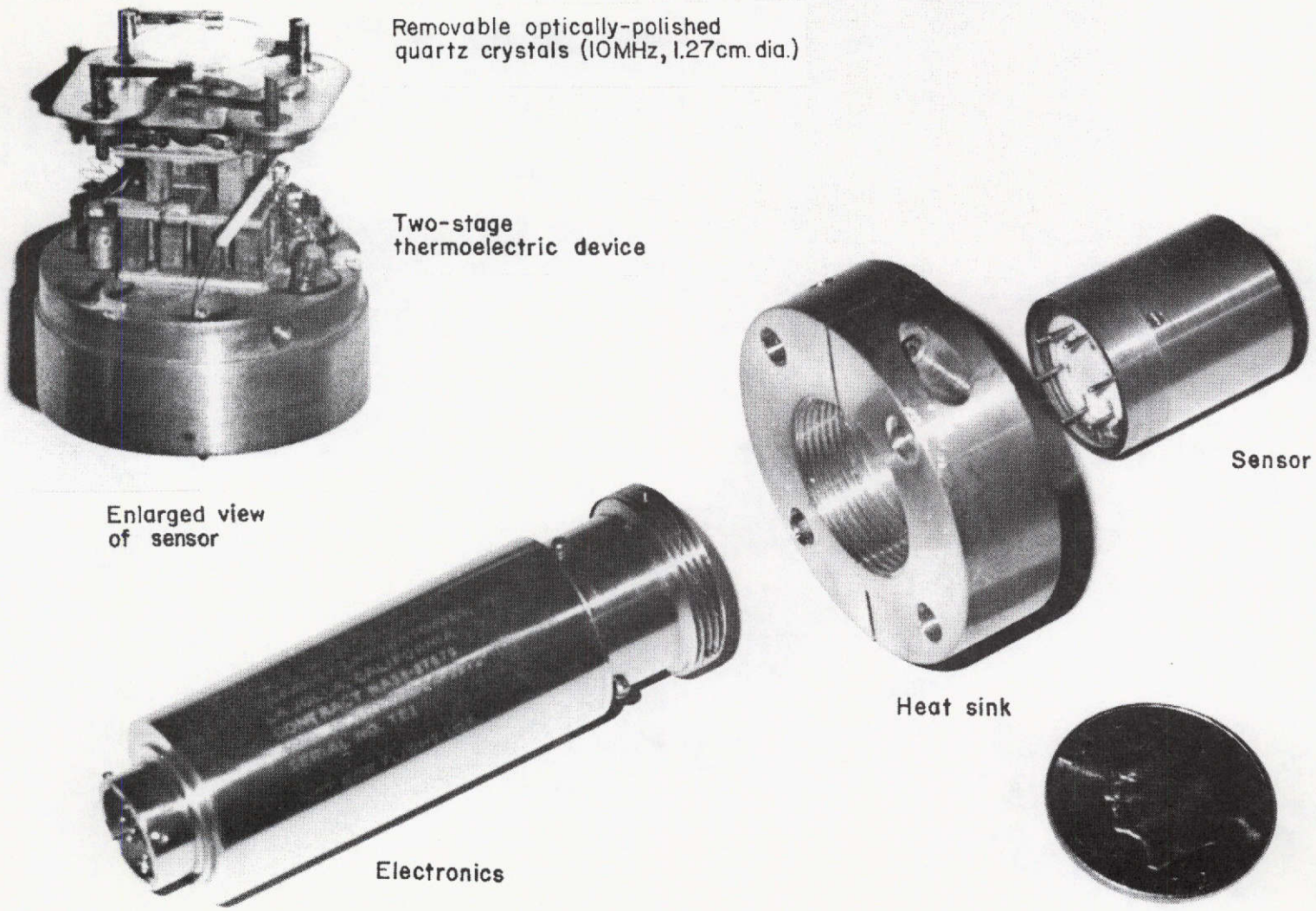

Fig. 3 TQCM Electronics, Heat Sink and Sensor

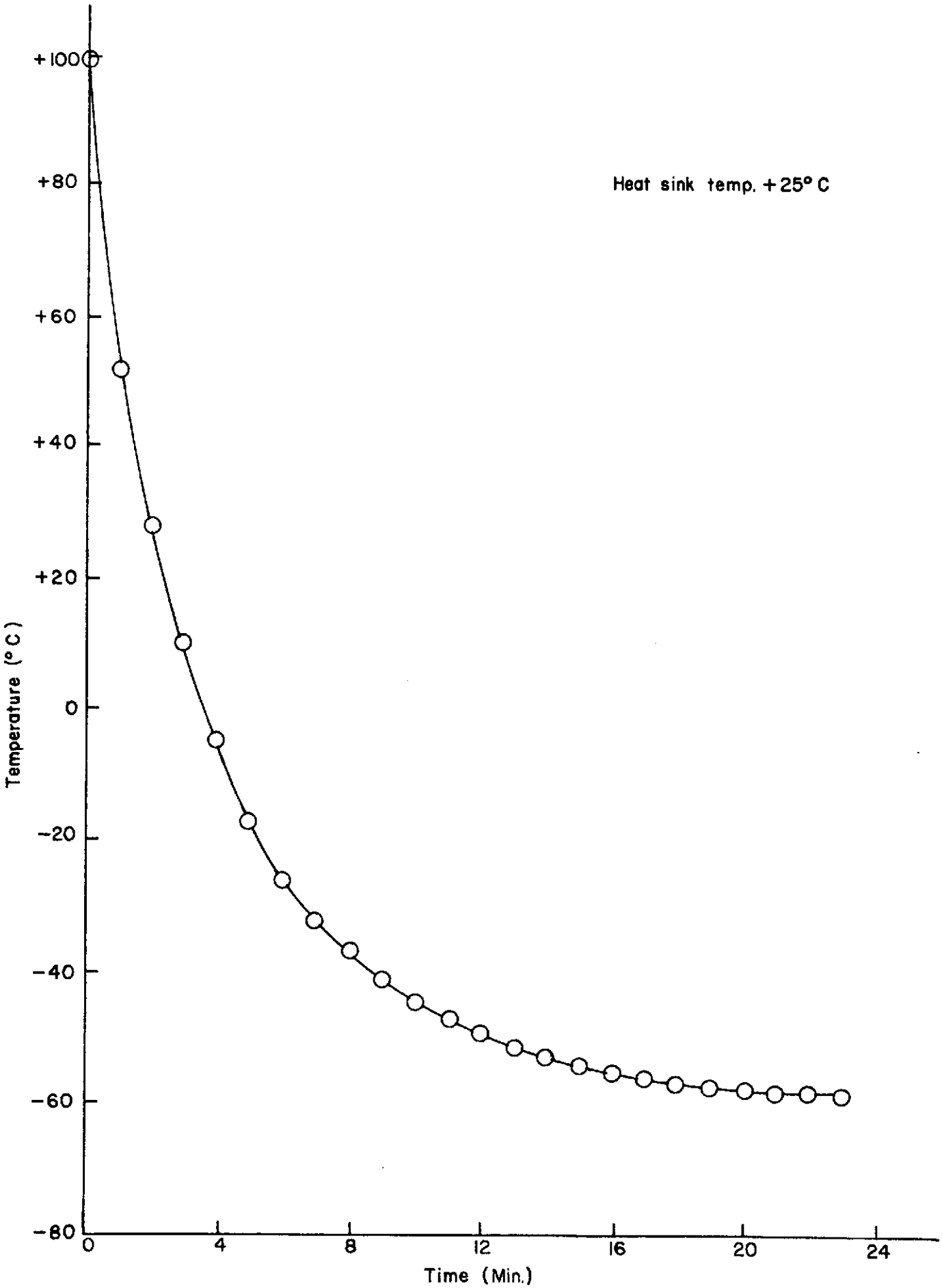

Fig. 4 TQCM cool-down time in vacuum from +100° C to -59° C

A frequency output is provided in the TQCM Controller to measure the frequency change of the crystal sensor produced by mass loading. Frequency is measured by a counter, such as, a Hewlett Packard Model HP5321B.

The TQCM can be set at any particular temperature over its operating range. If the TQCM is set at ambient, the heat generated in the oscillating crystal will be removed so that contamination loading to passive optical systems can be monitored. By increasing temperature to about +100°C the crystal can be cleaned. By periodically dropping the temperature of the TQCM in fixed steps, the amount of surface contamination for different equilibrium temperatures can be determined and the background level of contamination in a space simulation chamber monitored with time.

The TQCM can be used to generate a calibrated contamination flux so that the contamination sticking coefficients of surfaces can be measured. A TQCM calibrated source is generated as follows. Contamination from an uncalibrated source is directed at a TQCM cooled to -50°C. Contamination is allowed to freeze out on the TQCM. The uncalibrated source is then turned off and the vacuum system allowed to pump down. The TQCM now becomes the calibrated source by simply raising its temperature so that the contamination will desorb at the desired rate. By monitoring the TQCM frequency increase with time, the contamination mass flow rate can be accurately determined.

The TQCM can also be used to calibrate the mass loading of viscous films on the quartz crystal sensor that do not couple well into the oscillating mass of the crystal. As a contamination film grows to several hundred monolayers, its top layers will slip relative to the oscillating crystal. The simple relationship between mass loading and frequency change will not hold true. Calibration is achieved by dropping the sensor temperature to freeze the contamination and provide rigid mass coupling to the crystal.

CONTAMINATION MEASUREMENTS

Studies of background contamination in a vacuum chamber were made to show the capability of the TQCM to measure surface contamination under equilibrium conditions. A 150 l/sec Vac-Ion pump was used to evacuate the chamber to the 10^{-9} Torr range. Just prior to the measurements, the chamber was contaminated with Welsh Duo-Seal roughing pump oil that raised its pressure into the 10^{-7} Torr range.

The net mass gain or loss for an aluminum surface from the adsorption and desorption of background contamination present in the chamber at 7×10^{-7} Torr is shown in Fig. 5. Below -30°C adsorption predominated and contamination collected on the surface. Above -30°C desorption predominated. The break in the curve at about -10°C where the rate of desorption increased abruptly is significant.

The break shows a phase change occuring in the contamination from a solid to a liquid. The phase change caused a large increase in its vapor pressure and the higher desorption rate. We were unable to make a measurement at +20°C because the desorption rate became so large that by the time the surface reached +20°C the contamination was nearly completely desorbed.

Fig. 6 shows the desorption rate of roughing pump oil as a function of the number of monolayers on the surface for a contamination background pressure of 4×10^{-7} Torr. When the number of contamination layers reaches 200, the increase in the desorption rate starts to level off indicating the bulk properties of the oil predominate and the properties of the surface have little effect on the desorption. At 0°C the leveling off of the desorption rate is quite evident.

The desorption rate decreases rapidly as the number of layers present is reduced because of the higher bonding energy holding contamination layers near to the surface. The higher bonding energy results from contamination molecules filling cracks and crevices in the polycrystalline aluminum surface.

The number of monolayers of contamination on a surface in equilibrium with the contamination on the walls of the vacuum chamber as a function of temperature is shown in Fig. 7. The ambient temperature of the chamber was 23°C. The measurements were made by raising the TQCM temperature to +80°C to bake off surface contamination and then dropping its temperature to -50°C to adsorb a film of contamination. The TQCM temperature was then increased to a particular equilibrium temperature shown in the figure to determine the number of contamination monolayers. From the figure it can be seen that there was always oil contamination on the surface even at 4×10^{-7} Torr for temperatures below +30°C. It would have been impossible to make the measurements with a QCM because there are no net mass changes at equilibrium.

CONCLUSIONS

Most contamination is adsorbed on a surface in the gaseous

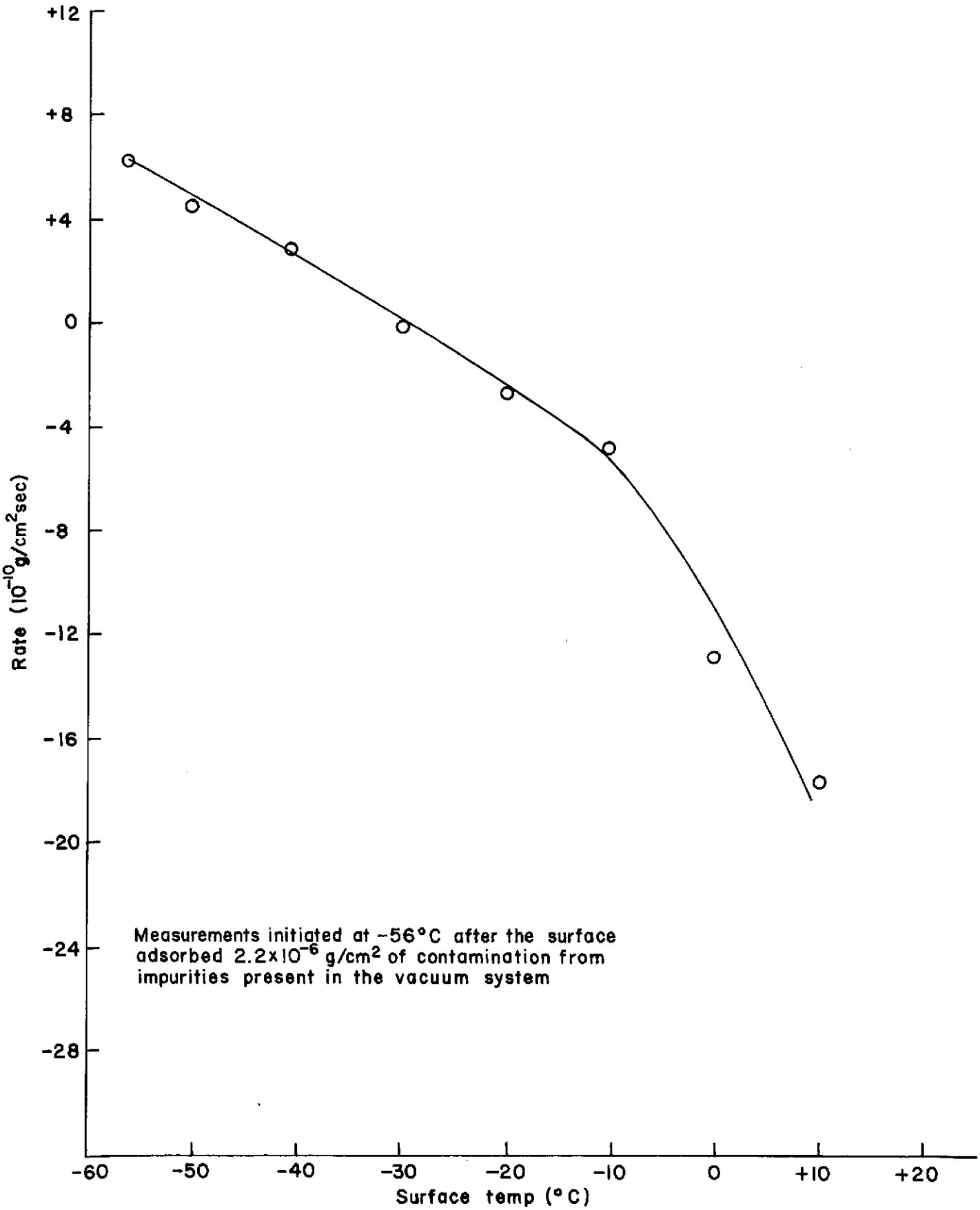

Fig.5 Contamination adsorption and desorption rates for an Al surface with temperature in a 7×10^{-7} Torr vacuum

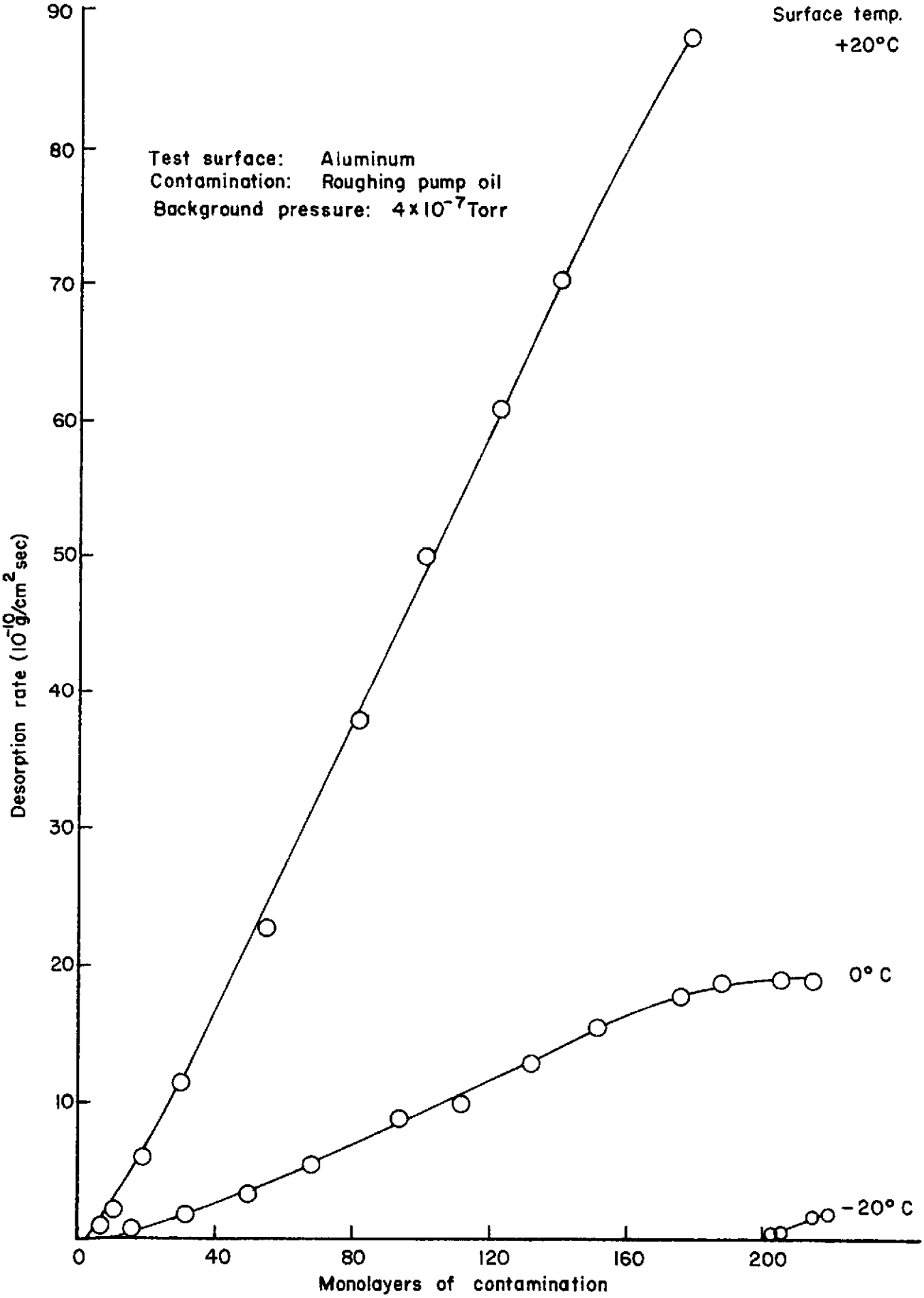

Fig.6 Contamination desorption rate as a function of monolayers on the surface

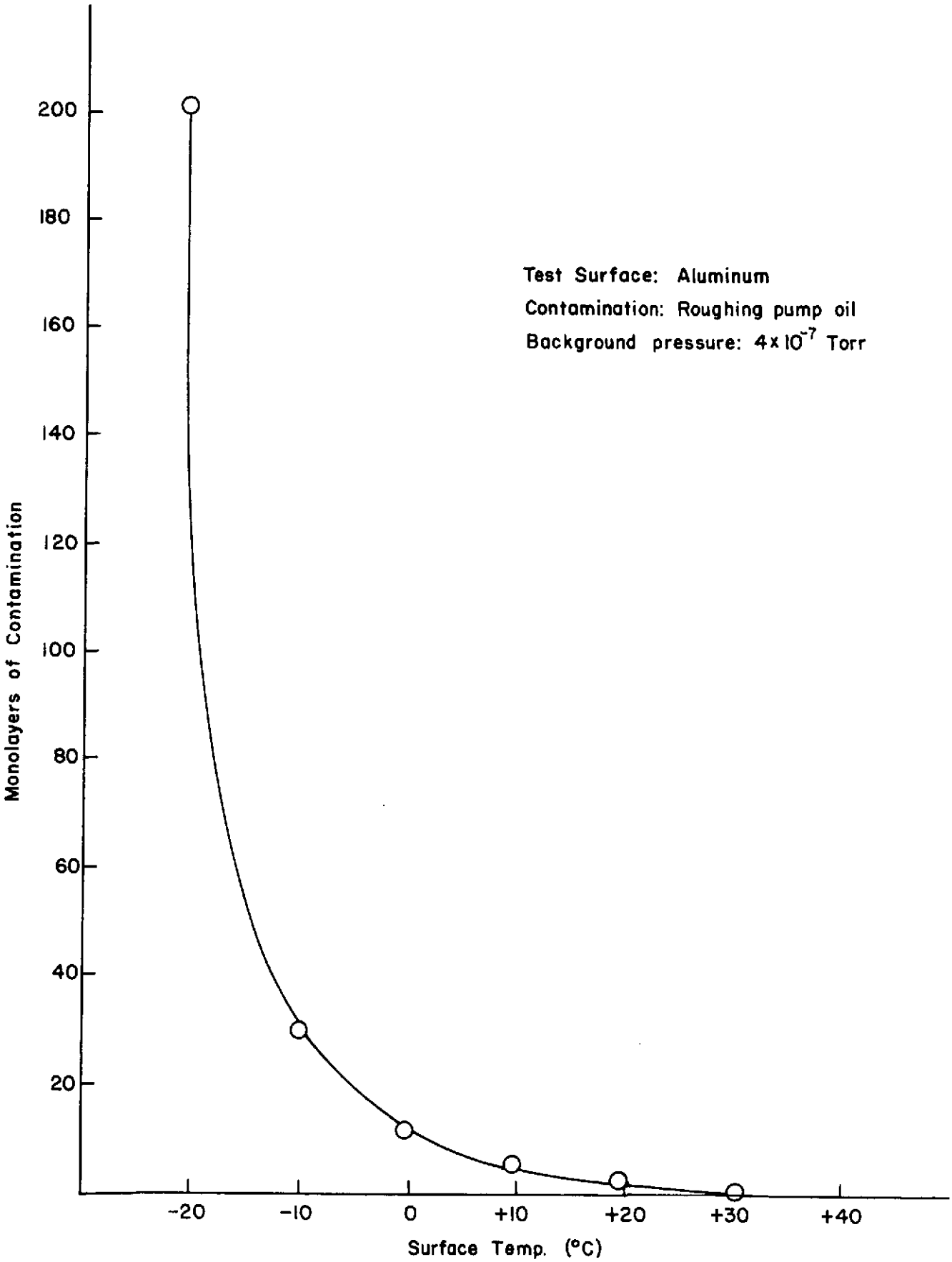

Fig. 7 Number of contamination monolayers on a surface at equilibrium

or liquid state and the adsorption rate is highly temperature dependent. A QCM is of limited value in monitoring contamination because it operates several degrees above ambient temperatures and does not readily adsorb contamination. For accurate measurements, a temperature controlled QCM should be used.

If a QCM is used to monitor contamination, measurements should be made from a directed source. The source temperature should be much higher than the QCM operating temperature to insure that the contamination sticking coefficient is greater than zero.

REFERENCES

1. Sauerbrey, G., "Application of Quartz Resonators for Weighing Thin Films and for Microweighing", Zeitschrift fur Physik, 155 206-222 (1959).

2. McKeown, D., "New Method for Measuring Sputtering in the Region Near Threshold", General Dynamics Convair Report ERR-AN-001, San Diego, Calif. (1959).

3. Vacuum Technology and Space Simulation, NASA SP-105, National Aeronautics and Space Administration, Washington, D.C.

4. Griffith, J.S., "Some Tests for Increase in Friction of Mechanisms of the Mariner Mars 1969 Spacecraft in the JPL Molsink Space Simulation Chamber", Proceedings of 4th Space Simulation Conference, AIAA/ASTM/IES, Los Angeles, Calif. (1969).

5. McKeown, D. and W.E. Corbin, Jr., "Space Measurements of the Contamination of Surfaces by OGO-6 Outgassing and Their Cleaning by Sputtering and Desorption", Space Simulation, NBS Special Publication 336, pp 113-127 (1970).

6. "Thermoelectrically-Cooled Quartz Crystal Microbalance", Operational Data, Faraday Laboratories Report FAR-73-101, La Jolla, Calif. (1973).